Journal of Physics D: Applied Physics

ACCEPTED MANUSCRIPT • OPEN ACCESS

$HCOO^-_{aq}$ Degradation in Droplets by OH_{aq} in an Atmospheric Pressure Glow Discharge

To cite this article before publication: Mackenzie Meyer *et al* 2023 *J. Phys. D: Appl. Phys.* in press https://doi.org/10.1088/1361-6463/acc958

$HCOO^-_{aq}$ Degradation in Droplets by OH_{aq} in an Atmospheric Pressure Glow Discharge

Mackenzie Meyer[1], Gaurav Nayak[2], Peter J. Bruggeman[2], Mark J. Kushner[1,3]

[1] University of Michigan, Electrical Engineering and Computer Science Department, 1301 Beal Ave., Ann Arbor, MI 48109-2122 USA maemeyer@umich.edu, mjkush@umich.edu
[2] University of Minnesota, Department of Mechanical Engineering, Minneapolis, MN, 55455 USA nayak025@umn.edu, pbruggem@umn.edu
[3] Author to whom correspondence should be addressed.

Abstract

Plasmas in contact with liquids can degrade organic molecules in solution, as reactive oxygen and nitrogen species produced in the plasma solvate into the liquid. Immersing small droplets (tens of microns in diameter) in the plasma can more rapidly activate the liquid compared to treating a large volume of liquid with a smaller surface-to-volume ratio. The interactions between a radio frequency glow discharge sustained in He/H_2O and a water droplet containing formate ($HCOO^-_{aq}$) immersed in and flowing through the plasma were modeled using a 0-dimensional global plasma chemistry model to investigate these activation processes. $HCOO^-_{aq}$ interacts with OH_{aq}, produced from solvation of OH from the gas phase. The resulting $HCOO^-_{aq}$ concentrations were benchmarked with previously reported experimental measurements. The diameter of the droplet, initial $HCOO^-_{aq}$ concentration, and gas flow rate affect only the $HCOO^-_{aq}$ concentration and OH_{aq} density, leaving the OH density in the gas phase unaffected. Power deposition and gas mixture (e.g., percentage of H_2O) change both the gas and liquid phase chemistry. A general trend was observed – during the first portion of droplet exposure to the plasma, OH_{aq} primarily consumes $HCOO^-_{aq}$. However, $O_2^-{}_{aq}$, a byproduct of $HCOO^-_{aq}$ consumption, consumes OH_{aq} once $O_2^-{}_{aq}$ reaches a critically large density. Using $HCOO^-_{aq}$ as a surrogate for OH_{aq} sensitive contaminants, combinations of residence time, droplet diameter, water vapor density, and power will determine the optimum remediation strategy.

I. Introduction

Atmospheric pressure plasmas in contact with liquids are used in a wide variety of applications, including water treatment, plasma electrolysis and plasma medicine [1–3]. These applications rely on plasma-produced reactive oxygen and nitrogen species (RONS) solvating into the liquid and chemically activating the liquid.

In most reactor configurations, transport limits the activation of the liquid through both solvation of the RONS in the gas into the liquid and transport of the RONS in the liquid. RONS produced in the plasma need to transport to the surface of the liquid to solvate. If the liquid is immersed in the plasma in the form of droplets, the distance between where the RONS are produced and the liquid can be shortened, and this transport limit can be mitigated. Once the RONS reach the surface of the liquid, these species need to transport from the surface into the bulk of the liquid. One way to mitigate this limit is to have a high surface-to-volume ratio (SVR) of the liquid, which decreases the time it takes for the RONS to transport from the surface into the bulk liquid. Using small water droplets (aerosols) in the plasma reduces both of the limits imposed by transport [4].

Experiments have shown how SVR influences the concentrations of RONS in the liquid. Hassan et al. compared the solvation of H_2O_2 (high Henry's law constant) and O_3 (low Henry's law constant) into bulk liquid and electrosprayed droplets [5]. They showed that increasing the surface area between the gas and liquid increased the concentration of H_2O_{2aq} and O_{3aq}. (The aq subscript denotes a solvated or aqueous species.) However, their results showed that the H_2O_{2aq} concentration was only 4 orders of magnitude larger than the O_{3aq} concentration, despite the difference in the Henry's law constants being 7 orders of magnitude. This difference was attributed to the depletion of H_2O_2 in the gas phase before the liquid reached Henry's law saturation. Liu et al. showed that the concentrations of long-lived RONS (H_2O_{2aq}, $NO_2^-{}_{aq}$, and $NO_3^-{}_{aq}$) and short-lived RONS ($ONOO^-{}_{aq}$ and $O_2^-{}_{aq}$) in water increase as the SVR increases [6]. Liu et al. further showed cancer cell containing media treated with plasma-activated water with a higher SVR was more effective at producing cell death, due to the higher concentrations of RONS in the solution.

Plasma has been proposed as an advanced oxidation process to remove organic pollutants from water [1]. Singh et al. used plasma sustained in Ar to treat landfill leachate samples containing PFAS [7]. The PFAAs and precursors were transported to the liquid surface by bubbling Ar through the liquid, forming a foam at the surface. Singh et al. showed that over 90%

of PFOA and PFOS and over 99.9% of long-chain PFAAs were degraded within 10 minutes of treatment by plasma. Jose and Philip used air plasma to degrade four toxic volatile organic compounds commonly found in pharmaceutical wastewater [8]. The water was sprayed into the plasma reactor and recirculated. For a hydraulic retention time of 33.3 min, over 90% of the four volatile organic compounds were removed. Using samples of pharmaceutical wastewater, instead of prepared solutions, over 90% of the volatile organic compounds were removed by plasma treatment. Jaiswal and Aguirre compared the effectiveness of He and Ar atmospheric pressure plasma jets (APPJs) on degrading methylene blue dye [9]. They observed that the Ar APPJ was more effective at degrading methylene blue compared to the He jet, an outcome they attributed to increased fluxes of oxygen radical onto the solution produced by the Ar APPJ. Casado et al. used an Ar plasma jet to degrade benzene present on top of a water layer [10]. They showed that phenol, catechol, and nitrobenzene were the main products formed from plasma interaction with benzene. These molecules are formed by benzene reactions with OH_{aq} and NO_{2aq}, likely formed by interactions between the ambient air and Ar excited states.

Sremacki et al. injected aerosol droplets (about 22 μm) into an Ar plasma jet to observe changes to the RONS and UV radiation from the plasma [11]. Aerosols in the plasma decreased the UV radiation by absorbing the radiation in the gas phase, and gas phase reactive oxygen species were also decreased. Products of the reactions between OH_{aq} and cysteine, used as a model biological molecule and dissolved in the aerosol, were detected. Cysteine conversion was highest when the bulk liquid was exposed to the plasma, presumably due to the increase in UV photons. Plasmas have also been shown to inactivate bacteria and viruses in solution. Xia et al. used a packed-bed dielectric barrier discharge to inactivate viruses in aerosols in the plasma [12]. At least 2.3 log reduction in the infectious virus concentration was observed in this reactor.

With the goal of investigating the transport of plasma produced ROS (reactive oxygen species) to droplets in a plasma, we have computationally investigated the degradation of formate ($HCOO^-_{aq}$), a model organic compound, by OH_{aq}, a short-lived reactive species produced by gas phase reactions and solvation into the droplet. The effect of in-droplet reactions such as UV/VUV photolysis are also discussed. $HCOO^-_{aq}$ is dissolved in a water droplet (tens of microns in diameter) immersed in an atmospheric pressure He/H_2O radio frequency glow discharge. Previous experimental work in this reactor is described in Nayak et al. and Oinuma et al. [13–16]. Nayak et al. measured the electron temperature and density in plasmas formed in this reactor sustained in

He and Ar, as well as He metastable densities [13,14]. In Oinuma et al., droplets with 2 mM $HCOO^-_{aq}$, produced by hydrolysis of formic acid $HCOOH_{aq}$, flowed through the He/H_2O plasma [15]. The droplets were exposed to OH formed in the gas phase which then solvates into the droplet. The $HCOO^-_{aq}$ concentration after exposure to the plasma was measured, and the change in $HCOO^-_{aq}$ concentration gave an estimate of OH transport into the droplet. Results of a 1-dimensional reaction-diffusion model showed that the interaction between OH_{aq} and $HCOO^-_{aq}$ happened primarily at the surface of the droplet. Nayak et al. investigated the effects of other reactive species on the $HCOO^-_{aq}$ concentration in the same reactor and found that another reactive species besides OH_{aq} that may consume $HCOO^-_{aq}$ is O_{aq} [16].

Using a global plasma chemistry model, the interactions between the plasma-produced ROS and a droplet were modeled for a reactor based on the experimental work by Nayak et al. and Oinuma et al. [13–16]. The global plasma chemistry model incorporates a local diffusion length from the plasma to the droplet and a reactive layer at the surface of the droplet. The base case (1 atm, He/H_2O=99.8/0.2, 14.3 W) has a water droplet 41 μm in diameter with an initial $HCOO^-_{aq}$ concentration of 2 mM and has a transit time of 10 ms through the plasma with an additional 10 ms flow time before collection. The consequences of plasma produced OH on $HCOO^-_{aq}$ degradation is discussed, as is the influence of photolysis of H_2O. In the liquid phase, the concentration of $HCOO^-_{aq}$ decreases due to reactions with OH_{aq} that consume the OH_{aq}. As the $HCOO^-_{aq}$ is decreased, the primary consumption of OH_{aq} changes to reactions with the products of $HCOO^-_{aq}$ degradation. The consequences of gas mixture, droplet diameter, initial $HCOO^-_{aq}$ concentration, flow rate (residence time), and power are discussed.

In Section II, the model and conditions used in this study are described, as well as a brief description of the experiments the modeling is based on. The plasma properties, and gas and liquid phase species densities are discussed in Section III. These properties are discussed in Section IV while varying droplet diameter, initial $HCOO^-_{aq}$ concentration, flow rate, power, gas mixture, and water percentage in the inlet gas mixture. Concluding remarks are shown in Section V.

II. Description of the Model and Experiments

This investigation was performed with the global plasma chemistry model *GlobalKin* to simulate conditions based on the experiments performed by Nayak et al. and Oinuma et al. [15,16]. The plasma reactor used by Nayak et al. and Oinuma et al. is an atmospheric pressure radio frequency glow discharge formed between two parallel plate electrodes separated by 2 mm and

which are 9.5 mm long. A schematic of the reactor is shown in Fig. 1a. Water droplets are released from a dispenser and pass through the plasma entrained in the gas flow, spending around 10 ms in the plasma depending on the flow rate of the gas. After flowing through the plasma, the droplets are frozen on an ultra-thin glass cover slip placed on an aluminum insert at the bottom of the reactor, which was kept at a temperature below freezing to preserve the exposed liquid for later chemical analysis. For the base case, a 2 mM solution of formic acid, $HCOOH_{aq}$, was used. The formic acid hydrolyzes to produce formate ($HCOO^-_{aq}$) and hydronium ($H_3O^+_{aq}$). $HCOO^-_{aq}$ reacts with OH_{aq} in the droplet, largely resulting from solvation of OH produced in the plasma. Measuring the change in the $HCOO^-_{aq}$ concentration gives a measure of the OH transport to the droplet. Further details on the experiments, including details of the measurements performed and the reactor, can be found in Nayak et al. and Oinuma et al. [13–16].

GlobalKin has been described previously in Lietz and Kushner [17] and so will be only briefly discussed here. As a global model, *GlobalKin* is 0-dimensional, with the gas and liquid phases treated as separate, well-mixed volumes. Each gas phase species has a matching liquid phase species, interacting by solvation of the gas phase species into the droplet or desolvation of the aqueous species into the gas phase. Each species density is determined by their individual rate equation, including sources and losses due to reactions and diffusion to surfaces. Charged particles diffuse to surfaces based on their ambipolar diffusion coefficient. The diffusion coefficient of negative ions is scaled by a Boltzmann factor to account for the negative ions having to climb the potential barrier intended to confine electrons. The electron energy conservation equation determines the electron temperature in the gas phase based on the specified power. As in this global model, power is specified, and there is no explicit dependence on, for example, RF frequency. Electron-impact rate coefficients are calculated by solving Boltzmann's equation for the electron energy distribution in the steady state.

Transport of species from the gas phase into the liquid occurs as a result of the liquid being treated as a surface in contact with the plasma. The loss of gas phase species to the liquid is then a function of the specified surface area of the liquid. For neutral species, Henry's law equilibrium determines the transport between the liquid and the gas. A diffusion flux of neutral species from the gas phase to the liquid is calculated. If the liquid is not saturated with the aqueous analogue of the gas phase species, a flux of gas phase species is allowed to diffuse into the liquid where the gas phase species is converted into its solvated analogue. If the liquid is super-saturated, there is

a desolvation flux of liquid phase species into the gas which are then converted back into gas phase species. Charged species directly solvate into the liquid. Evaporation of the liquid into the gas phase occurs by specifying a vapor pressure of the liquid at the surface of the droplet. Diffusion of the liquid vapor then occurs from the droplet into the bulk until the gas phase reaches the saturated vapor pressure.

GlobalKin allows for two diffusion lengths to account for transport processes to surfaces: one to solid surfaces in contact with the plasma, and one to the liquid in contact with the plasma. The diffusion length to surfaces in contact with the plasma is dominated by the parallel electrodes bounding the plasma, having a gap of 2 mm. Transport to these surfaces produces a diffusion length of 0.637 mm. Transport from the bulk plasma to the droplet is through a gas boundary layer surrounding the droplet, producing a diffusion length to the droplet of 100 μm.

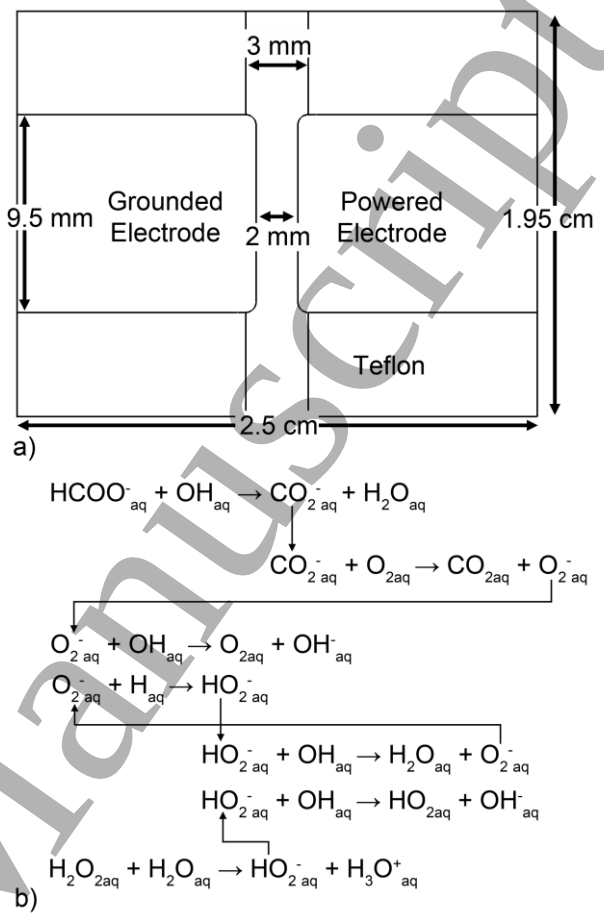

Figure 1. a) Schematic of the experimental reactor.[30] b) Schematic of the primary processes in the $HCOO^-_{aq}$ reaction mechanism.

The residence time of the droplet in the plasma, about 10 ms in the base case, is too short for solvating species to diffuse throughout the volume of the droplet. To account for the finite plasma exposure time, a reactive layer of finite thickness is specified at the droplet surface. Doing so divides the liquid volume into a surface layer in which plasma-initiated reactions occur and a nonreactive core. This formulation accounts for short-lived species in the droplet, in particular OH_{aq}, not being uniformly distributed throughout the droplet. These short-lived species are instead found near the droplet surface. As shown by Oinuma et al., the density of $HCOO^-_{aq}$ is degraded at the droplet surface while being only nominally changed in the center of the droplet [15]. Specifying the reactive layer thickness in *GlobalKin* therefore limits the amount of $HCOO^-_{aq}$ that

the OH_{aq} can interact with during the finite transit time of the droplet through the reactor. The species densities produced by *GlobalKin* are only for this reactive layer. In the experiments, the total average density of species in the droplet is measured. The total average density n_t in the droplet in the model is then calculated from

$$n_t = \frac{x_i\left(3.347\times10^{22}\,cm^{-3}\right)\left(V_c\right)+n_l V_l}{V_t}, \quad (1)$$

where x_i is the initial mole fraction of the species, 3.347×10^{22} cm^{-3} is the density of liquid water, V_c is the volume of the nonreactive core, n_l is the species density in the reactive layer, V_t is the total volume of the droplet, and $V_l = V_t - V_c$ is the volume of the reactive layer. If the species is not initially present in the solution (i.e., the initial mole fraction is zero), the total density is simply $n_l V_l/V_t$. There is no interaction between the reactive layer and the nonreactive core.

The reaction mechanism includes 112 gas phase species and 123 liquid phase species, listed in Table 1. Note that each gas phase species has a liquid phase counterpart, and some species only exist in the liquid. There are 3,027 gas phase reactions and 331 liquid phase reactions including reactions involving photons. The gas phase reaction mechanism is based on Van Gaens and Bogaerts [18] with updates to include He made by Norberg [19]. Updates were also made based on branching ratios to produce excited states in recombination of He^+ and He_2^+ from Emmert et al. [20]. Two gas mixtures examined include both He and Ar, and their interactions are included and based on Ref. [21]. The liquid phase reaction mechanism is based on Refs. [22] and [17]. The rates for interaction of He excited states and ions with H_2O_{aq} were estimated to be fast relative to other reactions and based on branching ratios from Refs. [22] and [23].

Additional reactions to address $HCOO^-_{aq}$ were included based on the reaction mechanism in Oinuma et al. [15]. In this reaction mechanism, $HCOO^-_{aq}$ is consumed by OH_{aq} and H_{aq}, producing H_2O_{aq} or H_{2aq} and $CO_2^-{}_{aq}$. Changes to the liquid phase reaction mechanism relative to Lietz and Kushner [17] are shown in Table 2. Henry's law constants are taken from Sander [24] and are listed in Table 3. A Henry's law constant greater than 1 indicates that, at equilibrium, the density of the species in the liquid will be larger than that in the gas. A Henry's law constant less than 1 means the density of the species in the gas will be larger than that in the liquid at equilibrium.

Photodissociation and photoionization of H_2O_{aq} are included in *GlobalKin*. UV/VUV photons are emitted from resonant states ($Ar(1s_2)$, $Ar(1s_4)$, Ar(4D), $He(2^1P)$, He(3P)) and dimer states (Ar_2^* and He_2^*) of noble gases. Photons are emitted with the natural lifetime of the state and

leave system based on transit time across the plasma. For the resonant states, photons are reabsorbed from the ground state to produce the corresponding resonant state. Using this technique, radiation trapping factors are not explicitly used but naturally result from the reabsorption and residence time of photons in the plasma. Reabsorption does not occur for the radiation emitted by dimers, as the dimers fragment into two ground state atoms upon emitting the photon and so have not absorbing ground state. To account for the small area of the droplet, the gas phase radiation in the plasma is shadowed by a flux that separately interacts with the H_2O_{aq} in the droplet. Sander et al. have showed that in liquid H_2O, the threshold for photoionization and photodissociation is lower than in the gas phase [25]. Therefore, all of the UV/VUV photons, including those emitted from Ar states, can interact with H_2O_{aq}. The UV/VUV photons photoionize H_2O_{aq}, producing $H_2O^+_{aq}$ and e_{aq}, and photodissociate H_2O_{aq}, producing H_{aq} and OH_{aq}.

The water droplets were prepared by dissolving equimolar amounts of formic acid $HCOOH_{aq}$ and $NaOH_{aq}$ into distilled water [15]. The initial conditions used in *GlobalKin* for the liquid includes 2 mM $H_3O^+_{aq}$, $HCOO^-_{aq}$, Na^+_{aq}, and OH^-_{aq}. To account for solvation of atmospheric gases, 2 s of exposure to air ($N_2/O_2/H_2O$ = 78/21/1) was simulated. The resulting aqueous mole fractions are shown in Table 4 for various initial concentrations of $HCOO^-_{aq}$ ($H_3O^+_{aq}$, Na^+_{aq}, and OH^-_{aq} were also adjusted to have the same initial concentration as $HCOO^-_{aq}$). $H_3O^+_{aq}$ and OH^-_{aq} have identical mole fractions that indicate a pH of 7. Na^+_{aq} and $HCOO^-_{aq}$ also have identical mole fractions. $HCOOH_{aq}$ is present at lower mole fractions than $HCOO^-_{aq}$. N_{2aq} and O_{2aq} have concentrations that indicate they are in Henry's law equilibrium with their gas phase counterparts. The mole fractions listed in Table 4 are used as initial conditions for the results discussed in Sections III and IV.

The simulations using *GlobalKin* address the volume between the electrodes in the reactor (19.1 mm × 9.5 mm × 2 mm). The flow rate varies from 0.75 slm – 3 slm, and the resulting residence times are shown in Table 5 [16]. The base case has a flow rate of 1 slm, corresponding to a residence time in the plasma of 10 ms. The power is specified as nearly a square wave in time, with a 0.1 ms ramp up and ramp down, and the power is kept constant for the residence time. The power varies depending on the gas mixture used, as shown in Table 6. The simulation ends after the plasma residence time plus 10 ms, the latter period to account for the flow of the gas and droplet to the collection surface. The electron temperature is set to 0.025 eV at 0.2 ms after the power has ramped down. Since the vast majority electrons have recombined or attached by this time, this

assignment of electron temperature does not affect the results of the simulation but does eliminate numerical problems. (Electron temperature in the simulation is obtained from dividing electron energy density by electron density. When both electron energy density and electron density trend towards zero, the system becomes numerically stiff.) Each gas mixture includes impurities as measured in Nayak et al. (2.3 ppm H_2O, 1.5 ppm O_2, and 6.0 ppm N_2) [14]. While these impurities were measured in pure He, they were applied to all gas mixtures in this study.

III. Degradation of $HCOO^-_{aq}$ by OH_{aq}

The reaction mechanism in the liquid primarily involves $HCOO^-_{aq}$, OH_{aq}, $CO_2^-_{aq}$, $O_2^-_{aq}$, and $HO_2^-_{aq}$. A schematic representation of the dominant reactions in the mechanism is in Figure 1. The $HCOO^-_{aq}$ dissolved in the droplet undergoes a reaction with OH_{aq}, forming $CO_2^-_{aq}$ and H_2O_{aq}. This reaction is the dominant consumption mechanism of OH_{aq} in the liquid during the first part of the residence time. While $HCOO^-_{aq}$ also reacts with H_{aq}, this reaction is much less important than the reaction with OH_{aq} due to the order of magnitude lower rate coefficient and order of magnitude lower density of H_{aq} due to its smaller Henry's law constant. During the second part of the residence time, OH_{aq} reacts with the byproducts of $HCOO^-_{aq}$ degradation. Once the power turns off (or equivalently, the droplet exits the plasma region), and the source of OH_{aq} from solvation from the gas phase decreases, the reactions with the byproducts of $HCOO^-_{aq}$ degradation will usually consume the remaining OH_{aq}. The $CO_2^-_{aq}$ that is formed from the reaction of OH_{aq} and $HCOO^-_{aq}$ then reacts with O_{2aq} in a charge-exchange reaction, forming CO_{2aq} and $O_2^-_{aq}$. As O_{2aq} is not a reactive species and is instead found in the liquid due to the initial conditions (Table 4) or due to solvation of the impurity, the charge-exchange reaction occurs when $CO_2^-_{aq}$ is available.

Once the density of $CO_2^-_{aq}$ increases and the corresponding increase in $O_2^-_{aq}$ occurs, $O_2^-_{aq}$ reacts directly with OH_{aq}. The reaction of $O_2^-_{aq}$ and OH_{aq} becomes the dominant consumption mechanism of OH_{aq} when the density of $O_2^-_{aq}$ increases. Since the rate coefficient of OH_{aq} reacting with $O_2^-_{aq}$ is approximately 3 times larger than the rate coefficient of OH_{aq} reacting with $HCOO^-_{aq}$, the reaction with $O_2^-_{aq}$ becomes the dominant consumption mechanism when the density of $O_2^-_{aq}$ is more than 33% of the $HCOO^-_{aq}$. $O_2^-_{aq}$ can also react with H_{aq} to produce $HO_2^-_{aq}$; however, the dominant formation mechanism of $HO_2^-_{aq}$ is a reaction of H_2O_{2aq} with H_2O_{aq}. $HO_2^-_{aq}$ can further react with OH_{aq} in two reactions: a charge-exchange to form HO_{2aq} and OH^-_{aq} or a reaction to form H_2O_{aq} and $O_2^-_{aq}$.

The base case examines the degradation of $HCOO^-_{aq}$ in a 41 μm diameter droplet exposed to a plasma sustained in He/H_2O = 99.8/0.2 (with impurities). The flow rate is 1 slm, corresponding to a residence time of 10 ms. The power deposition is 14.3 W. The droplet initially contains 2 mM $HCOO^-_{aq}$.

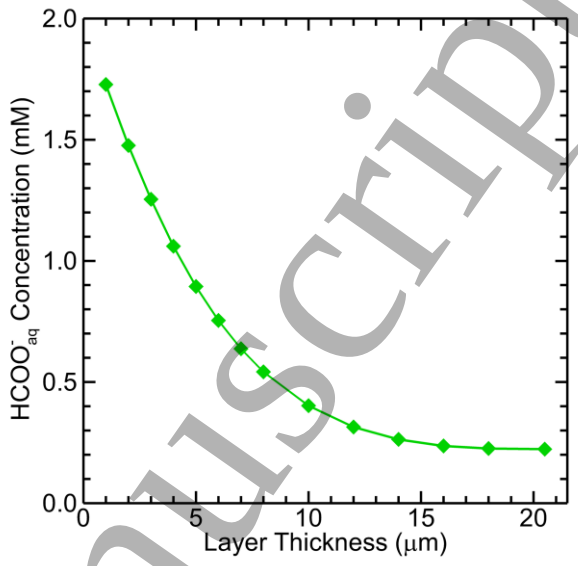

Figure 2. $HCOO^-_{aq}$ concentration at the time of collecting the droplet for varying droplet reactive layer thicknesses at 1 slm flow rate. The concentration is averaged over the droplet.

A. Reactive Layer Thickness

Before investigation of the $HCOO^-_{aq}$ degradation and reactive species densities, the thickness of the reactive layer was determined. The droplet is divided into two zones: the reactive layer and the nonreactive core. The reactive layer and nonreactive core do not interact throughout the simulation. The thickness of the reactive layer limits the amount of $HCOO^-_{aq}$ that can be consumed by OH_{aq} during the transit of the droplet through the reactor. The thickness of the reactive layer was determined by performing simulations varying the thickness from 1 μm to 20.5 μm, where for the maximum thickness the entire droplet is considered reactive. The reactive layer thickness was then chosen to best match the experimental measurements of droplet averaged concentration of 0.76 mM $HCOO^-_{aq}$ remaining after plasma treatment.

The remaining $HCOO^-_{aq}$ concentrations after plasma activation and post-plasma flow for varying reactive layer thicknesses are shown in Figure 2. As the reactive layer thickness increases, the volume of the reactive layer increases compared to the nonreactive core, and the total inventory of $HCOO^-_{aq}$ in the reactive layer increases. As the amount of $HCOO^-_{aq}$ in the reactive layer increases, more $HCOO^-_{aq}$ can be consumed by OH_{aq} during the residence time of the droplet in the plasma. The reactive layer thickness that best matches the experimental measurements is 6 μm, with a remaining droplet averaged $HCOO^-_{aq}$ concentration of 0.75 mM. 6 μm was used as the reactive layer thickness at 1 slm, which agrees well with the 1-dimensional simulations of Oinuma et al. [15]. This reactive layer thickness is similar to the diffusion length in the 10 ms residence

time. The diffusion length is proportional to $\sqrt{tD}$, where t is the time and D is the diffusion coefficient. The diffusion length in the liquid is 3.8 μm for this system, similar to the 6 μm reactive layer thickness determined to best match experimental measurements.

B. Plasma Properties and Reactive Species Densities

The plasma properties for the base case are shown in Figure 3a. The electron density is initialized at 10^8 cm^{-3}. As the power ramps up, the electron temperature increases and is maximum at 0.15 μs at 3.7 eV, avalanching the plasma. As the power continues ramping up over 0.1 ms, the electron density increases, and the electron temperature slightly decreases. After about 3.5 ms, a steady state is reached in both the electron temperature and density, 1.8×10^{11} cm^{-3} and 2.6 eV. After the power ramps down, the electrons are quickly consumed primarily by dissociative recombination as the electron temperature decreases.

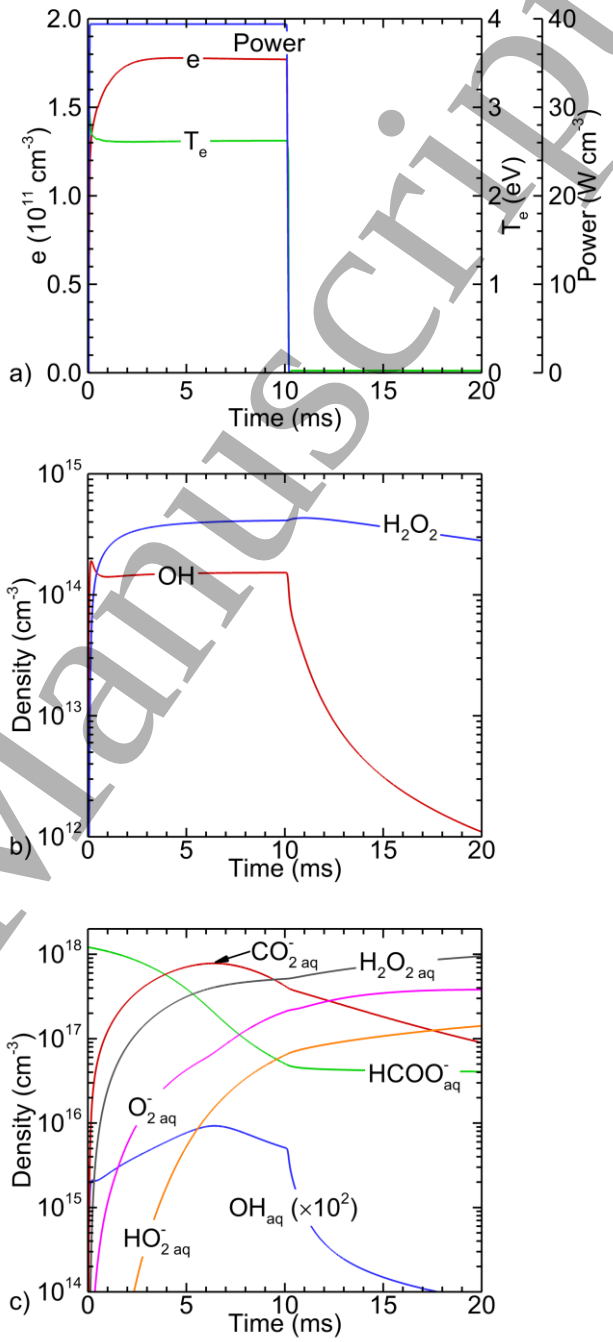

Figure 3. Droplet and plasma properties for the base case. a) plasma properties, b) gas phase species densities, and c) liquid phase species densities in the reactive layer of the droplet.

The densities of OH and H_2O_2 in the gas phase are shown in Figure 3b. When the power first turns on, the density of OH rapidly increases to 1.9×10^{14} cm^{-3} due to electron-impact dissociation of H_2O. At the location of the maximum in the density of OH, the electron temperature is higher than its steady

state value, and the electron density is increasing to its steady state value, leading to an increase in OH production. As the electron density and temperature reach their steady state values, the density of OH slightly decreases to its steady state value of 1.5×10^{14} cm^{-3}, balancing losses due to reactions and solvation into the droplet and the source of OH due to electron-impact dissociation of H_2O. Once the power turns off, and the electron temperature and density rapidly decrease, the production of OH by electron-impact dissociation ceases. The remaining OH is rapidly consumed due to reactions which form H_2O_2, H_2O, or O_2.

When the power first turns on, the density of H_2O_2 rapidly increases, formed primarily by OH reacting with OH. The density of H_2O_2 then reaches a steady state value near 4.1×10^{14} cm^{-3}. While OH continues to produce H_2O_2 throughout the power on period, H_2O_2 has a high Henry's law constant (1.92×10^6), meaning H_2O_2 will readily solvate into the liquid. Immediately after the power turns off, the H_2O_2 density increases slightly. After 12 ms, H_2O_2 begins to decrease as solvation into the droplet continues depleting H_2O_2 in the gas phase while the source of H_2O_2 by reactions of OH decreases.

The densities of OH_{aq}, $HCOO^-_{aq}$, H_2O_{2aq}, $CO_2^-{}_{aq}$, $O_2^-{}_{aq}$, and $HO_2^-{}_{aq}$ are shown in Figure 3c. These densities are shown in the reactive layer only and are not scaled to a droplet average as described by Eq. 1. The density of OH_{aq} increases rapidly during the first 0.2 ms, due to solvation of gas phase OH. The density of OH_{aq} increases throughout the first 6.4 ms. The gas phase plasma supplies a nearly constant source of OH, and since OH has a moderately high Henry's law constant of 620, OH readily solvates into the droplet. Photodissociation is not an important source of OH_{aq} due to the low densities of emitting He states which are quenched by reactions with H_2O and impurities. In the first 5.5 ms, the main consumption mechanism of OH_{aq} in the droplet is its reaction with $HCOO^-_{aq}$. As the $HCOO^-_{aq}$ density decreases in the reactive layer due to reactions with OH_{aq}, the OH_{aq} density increases because its rate of consumption decreases. The density of OH_{aq} reaches a maximum at 6.4 ms, or 3.7 ms before the power begins ramping down, at a value of 9.3×10^{13} cm^{-3}. At this point, much of the $HCOO^-_{aq}$ in the reactive layer has been consumed. The density of $CO_2^-{}_{aq}$ increases as it is a reaction product of OH_{aq} with $HCOO^-_{aq}$. Due to the increase in $CO_2^-{}_{aq}$, $O_2^-{}_{aq}$ increases through a charge-exchange reaction with O_{2aq}. $HO_2^-{}_{aq}$ increases through reactions between H_2O_{2aq} and H_2O_{aq}, as well as H_{aq} and $O_2^-{}_{aq}$. The dominant consumption mechanisms of OH_{aq} are then through reactions with $O_2^-{}_{aq}$ and, to a lesser extent, $HO_2^-{}_{aq}$, not $HCOO^-_{aq}$. The density of $HCOO^-_{aq}$ is 3 times that of $O_2^-{}_{aq}$ at 6.4 ms; therefore, the rates of OH_{aq}

consumption by $HCOO^-_{aq}$ and $O_2^-_{aq}$ are comparable. When the power turns off, there is no longer a source of OH in the gas phase plasma that replenishes the consumed OH_{aq}, and the density of OH_{aq} rapidly decreases.

The density of $HCOO^-_{aq}$ decreases through most of the power on period due to the consumption of $HCOO^-_{aq}$ by OH_{aq}. At 6.4 ms, the $HCOO^-_{aq}$ density in the reactive layer is 2.0×10^{17} cm^{-3}, only 20% of its initial value of 1.2×10^{18} cm^{-3}. However, when the $HCOO^-_{aq}$ in the nonreactive core is included, the total $HCOO^-_{aq}$ density in the droplet is 6.0×10^{17} cm^{-3} at 6.4 ms. Depletion of $HCOO^-_{aq}$ continues to occur even after OH_{aq} begins decreasing. $HCOO^-_{aq}$ reaches a concentration of 4.9×10^{16} cm^{-3} in the reactive layer at 10.1 ms, when the power begins to decrease. Overall, the $HCOO^-_{aq}$ concentration averaged over the droplet decreases from 2 mM at the beginning of the simulation to 0.75 mM at the end of the simulation.

H_2O_{2aq} density increases throughout the power on period because there is a source of H_2O_2 in the gas phase plasma and H_2O_{2aq} has a high Henry's law constant. After the power turns off, the H_2O_{2aq} density again increases, due to the formation of H_2O_2 and H_2O_{2aq} by OH and OH_{aq}. The H_2O_{2aq} density increases through the end of the simulation as gas phase H_2O_2 solvates into the liquid.

$CO_2^-_{aq}$ is one of the products from the reaction of $HCOO^-_{aq}$ and OH_{aq} (the other product is H_2O_{aq}). Therefore, while the $HCOO^-_{aq}$ density decreases, the $CO_2^-_{aq}$ density increases. $CO_2^-_{aq}$ reaches a maximum density at 6.4 ms of 7.8×10^{17} cm^{-3} in the reactive layer, coinciding with when the $HCOO^-_{aq}$ density decrease slows and the maximum in OH_{aq} occurs. Once the consumption of $HCOO^-_{aq}$ slows, the source of $CO_2^-_{aq}$ also slows, and the $CO_2^-_{aq}$ density decreases through the charge exchange reaction with O_{2aq} that produces $O_2^-_{aq}$.

$O_2^-_{aq}$ is primarily produced through the charge exchange reaction with $CO_2^-_{aq}$ and O_{2aq}. Therefore, $O_2^-_{aq}$ density increases throughout the simulation. The main consumption mechanism of $O_2^-_{aq}$ is reacting with OH_{aq} to produce O_{2aq} and OH^-_{aq}.

$HO_2^-_{aq}$ is primarily produced by reactions between H_2O_{2aq} and H_2O_{aq} and by reactions between H_{aq} and $O_2^-_{aq}$. During the first 10 ms, $HO_2^-_{aq}$ increases rapidly, as H_2O_{2aq} is plentiful and the source of H_{aq} from the gas phase is high. However, after the power turns off, the source of H_{aq} stops due to depletion of H in the gas phase, and the H_{aq} density decreases, limiting the amount of $HO_2^-_{aq}$ formed. Therefore, the increase in $HO_2^-_{aq}$ after the power turns off is due dominantly to H_2O_{2aq} and H_2O_{aq}.

The results from the model are compared to the experimental measurements in Table 7. The electron density and temperature are reactor averaged values, while the experimental values result from optical emission measurements emphasizing properties where the He atoms are excited [13]. Given these differences, agreement is good. The OH density and $HCOO^-_{aq}$ concentration are also shown in Table 7. The $HCOO^-_{aq}$ concentration predicted by the model is averaged over the reactive layer and nonreactive core as described by Eq. 1. The model underpredicts the measured OH density by a factor of two. In the global model, any OH in the gas phase can solvate into the droplet. Since OH does not reach Henry's law equilibrium in the droplet, OH in the gas phase constantly solvates into the liquid phase in the model. However, in the experiments, OH must be near the droplet to solvate into the droplet, resulting in local depletion of the OH. This limits the amount of OH that can solvate into the droplet and increases the OH in the gas phase relative to the model. The $HCOO^-_{aq}$ concentration predicted by the model matches the experimental measurements well, as the reactive layer thickness was chosen to match the measured $HCOO^-_{aq}$ concentration.

IV. OH, OH_{aq}, and $HCOO^-_{aq}$ Variation with Liquid and Plasma Properties

The decomposition of $HCOO^-_{aq}$ in the droplet depends on the properties of the droplet and the plasma. In this section, properties of the droplet (diameter and initial $HCOO^-_{aq}$ concentration) and of the plasma (gas flow rate, power deposition, gas mixture) are varied, and the effects on the densities of OH, OH_{aq}, and $HCOO^-_{aq}$ are discussed. The reactive layer thickness was kept constant at 6 μm at all flow rates of 1 slm.

A. Droplet Diameter

Varying the droplet diameter varies the total inventory of $HCOO^-_{aq}$ in the droplet and therefore also varies the time required to consume $HCOO^-_{aq}$. The reactive layer thickness was kept constant at 6 μm regardless of diameter.

The variation of the density of OH with droplet diameter and SVR is shown in Figure 4. OH density was recorded at 10.1 ms, the time that the power begins to ramp down, corresponding to the time the droplet exits the plasma. The OH density does not significantly vary with droplet diameter or SVR and is nearly constant at 1.5×10^{14} cm^{-3}. Therefore, increasing the droplet diameter does not significantly affect the gas phase plasma. In particular, droplet diameter does

not affect the H_2O density in the gas phase. This is because the majority of H_2O in the gas phase does not come from evaporation of the droplet; rather, it comes from the 0.2% H_2O in the gas mixture.

While the gas phase OH does not vary with droplet diameter or SVR, OH_{aq} and $HCOO^-_{aq}$ do vary with droplet diameter and SVR, as shown in Figure 4. Both the OH_{aq} density and $HCOO^-_{aq}$ concentration are averaged over the reactive layer and nonreactive core, as described by Eq. 1. OH_{aq} density was recorded at 10.1 ms, and $HCOO^-_{aq}$ concentration in the droplet was calculated after an additional 10 ms corresponding to flow to the collector. For all droplet diameters, $HCOO^-_{aq}$ density in the reactive layer was low, decreasing to 6.3 × 10^{16} cm^{-3} for an 81 μm diameter droplet and 1.7 × 10^{16} cm^{-3} for a 21 μm diameter droplet at the end of the simulation. The $HCOO^-_{aq}$ density in the nonreactive core of the droplet remains constant at 1.2 × 10^{18} cm^{-3}. With small droplet diameters, the reactive layer constitutes most of the volume of the droplet (i.e., at 21 μm, the reactive layer is 92% of the total droplet volume). However, as the droplet diameter increases, the reactive layer is progressively a smaller fraction of the volume of the droplet, decreasing to 38% of the total droplet volume at a diameter of 81 μm. Therefore, as diameter increases (SVR decreases), the $HCOO^-_{aq}$ concentration remaining in the droplet becomes more

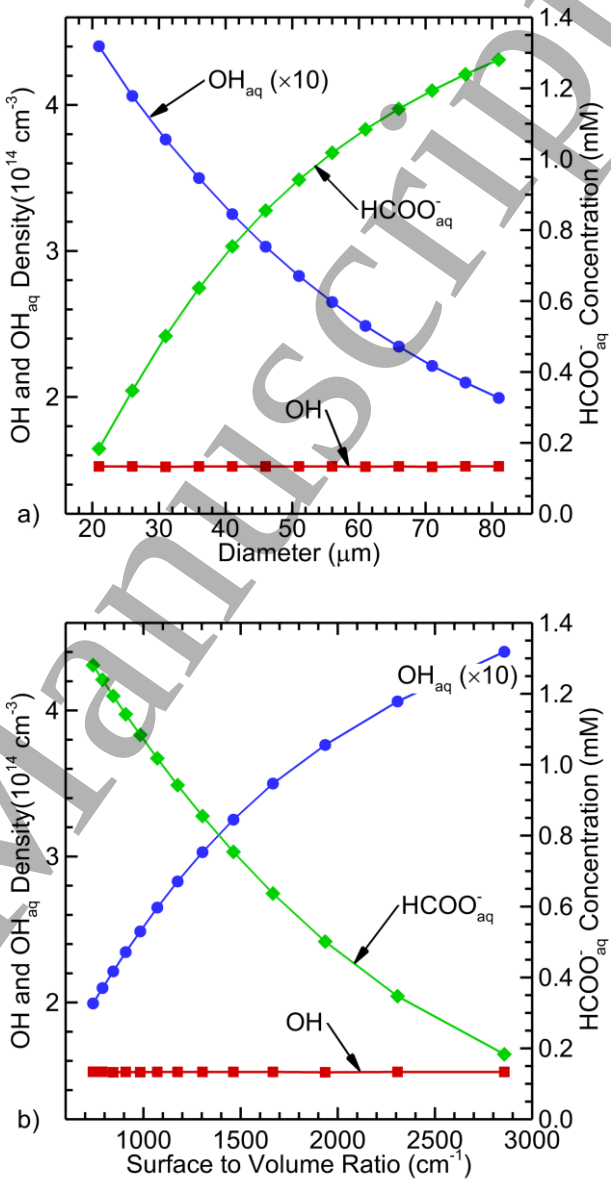

Figure 4. OH, OH_{aq} and $HCOO^-_{aq}$ densities as a function of surface to volume ratio of the droplet. The densities of OH, OH_{aq} are when the power begins to ramp down (10.1 ms), corresponding to the droplet exiting the plasma. $HCOO^-_{aq}$ concentration is after an additional 10 ms, for flow to the collector. Aqueous quantities are averaged over the droplet.

dependent on the concentration in the core and therefore increases. This variation is in fact linear with SVR.

OH_{aq} is only present in the reactive layer and not in the nonreactive core of the droplet. Therefore, its density is scaled by the volume of the reactive layer over the total volume. As the diameter increases, OH_{aq} in the reactive layer peaks later and at smaller densities during the power on period. However, as the power begins to turn off at 10.1 ms, OH_{aq} in the reactive layer increases as diameter increases. This increase occurs because $O_2^-{}_{aq}$ in the reactive layer decreases as diameter increases, consuming less OH_{aq}. However, when averaged over the reactive layer and nonreactive core as shown in Figure 3, OH_{aq} decreases as diameter increases. As diameter increases, the relative volume of the nonreactive core compared to the reactive layer increases, decreasing the droplet-averaged density. This variation is again linear with SVR.

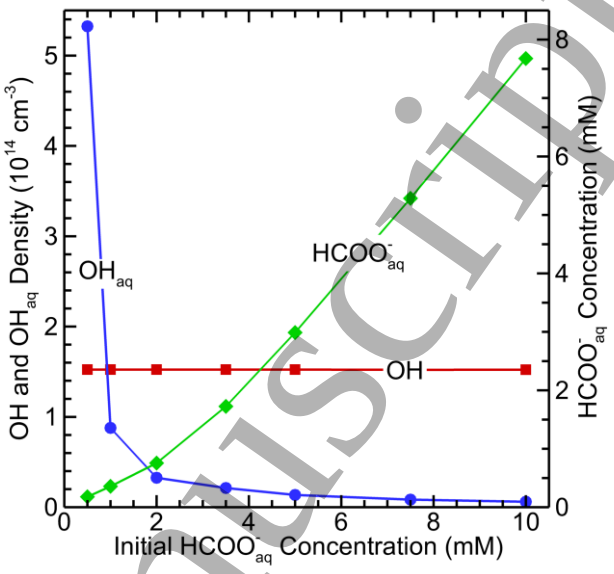

Figure 5. Reactive species densities as a function of initial $HCOO^-_{aq}$ concentrations. OH and OH_{aq} densities are shown as the power begins to ramp down (10.1 ms) corresponding to the droplet leaving the plasma. $HCOO^-_{aq}$ concentration is shown after an additional 10 ms for flow to the collector. Aqueous quantities are averaged over the droplet.

The $HCOO^-_{aq}$ concentrations in the droplet are compared to the experimental measurements in Table 8 for three different droplet diameters. At 36 µm and 41 µm, the $HCOO^-_{aq}$ concentrations predicted by the model match the measurements within uncertainty. However, at 56 µm, the model predicts 1.02 mM of $HCOO^-_{aq}$ remaining, while the measurements show 1.61 mM of $HCOO^-_{aq}$ remaining. This discrepancy may be a consequence of the effective reactive layer thickness being smaller for a diameter of 56 µm as can be deduced from $HCOO^-_{aq}$ diffusion profiles calculated by a 1D model [15].

B. Initial $HCOO^-_{aq}$ Concentration

Varying the initial concentration of $HCOO^-_{aq}$ in the droplet varies the total inventory of $HCOO^-_{aq}$ in the droplet and the time required to consume $HCOO^-_{aq}$ for otherwise constant plasma

conditions. The initial concentration of $HCOO^-_{aq}$ also changes the initial mole fractions of $HCOO^-_{aq}$, Na^+_{aq}, and $HCOOH_{aq}$, as shown in Table 4.

The variation of the density of OH with initial $HCOO^-_{aq}$ concentration is shown in Figure 5 as the power begins to ramp down (10.1 ms) when the droplet leaves the plasma. The OH density does not significantly vary with initial $HCOO^-_{aq}$ concentration, demonstrating that gas phase plasma is not strongly affected by the initial composition of the droplet. In order for the composition of the droplet (of fixed diameter) to affect the gas properties, the rate of solvation of a gas phase species (or desolvation of an aqueous species) would need to significantly change with initial concentration. This would require that the aqueous analogue of a gas species becomes saturated (or supersaturated) in the droplet in a manner that is sensitive to the initial concentration. This would likely occur only for species having small Henry's law constants. Since the gas phase species of interest (i.e., OH, H_2O_2) have moderate to large Henry's law constants and do not saturate in the droplet, gas phase properties are not sensitive to the initial $HCOO^-_{aq}$ concentration.

While the gas phase density of OH does not vary with initial $HCOO^-_{aq}$ concentration, OH_{aq} at the time the power begins to ramp down (10.1 ms), or exit from the plasma, and $HCOO^-_{aq}$ after an additional 10 ms of flow time do vary, as shown in Figure 5. The densities of OH_{aq} and $HCOO^-_{aq}$ were averaged over the droplet as described in Eq. 1. At low initial $HCOO^-_{aq}$ concentrations (0.5 mM and 1 mM), $HCOO^-_{aq}$ in the reactive layer is decreased below 10^{15} cm^{-3} by the time of collection. The total $HCOO^-_{aq}$ concentration is then dominated by the concentration in the nonreactive core. The density of $HCOO^-_{aq}$ in the reactive layer is also decreased earlier at low initial $HCOO^-_{aq}$ concentrations, and the maximum in the density of OH_{aq} occurs earlier. Following the maximum, OH_{aq} is consumed by reactions with $O_2^-{}_{aq}$, depleting $O_2^-{}_{aq}$ before the power turns off. The OH_{aq} then increases after $O_2^-{}_{aq}$ is depleted by solvation of gaseous OH.

For initial $HCOO^-_{aq}$ concentrations of 2 mM and 3.5 mM, the density of $HCOO^-_{aq}$ decreases in the reactive layer by at least 75%, but $O_2^-{}_{aq}$ has a density at least 33% of the $HCOO^-_{aq}$ concentration before the power turns off and begins consuming OH_{aq}. As the initial $HCOO^-_{aq}$ concentration increases, more $HCOO^-_{aq}$ remains in the reactive layer after plasma treatment. In fact, at 10 mM initial $HCOO^-_{aq}$ concentration, the remaining density in the reactive layer is 4×10^{18} cm^{-3} (initial density is 6×10^{18} cm^{-3}). Therefore, the total $HCOO^-_{aq}$ concentration is not only due to the nonreactive core; the reactive layer still has a significant amount of $HCOO^-_{aq}$ remaining. Above an initial $HCOO^-_{aq}$ concentration of 5 mM, at least 2 mM of $HCOO^-_{aq}$ is degraded by OH_{aq}.

Since $HCOO^-_{aq}$ is not depleted in the reactive layer at high initial $HCOO^-_{aq}$ concentrations, the density of OH_{aq} density is low, as it is still actively being consumed in the reaction with $HCOO^-_{aq}$. The density of $O_2^-{}_{aq}$ is over a factor of 3 lower than $HCOO^-_{aq}$, implying that the consumption of OH_{aq} by $O_2^-{}_{aq}$ is not dominant.

C. Gas Flow Rate

Varying the gas flow rate changes the residence time of the droplet in the plasma. At low gas flow rates, the residence time of the droplet in the plasma is long; at high gas flow rates, the residence time of the droplet in the plasma is short. The flow rates and corresponding residence times are listed in Table 5 and are primarily taken from the experimental work in Nayak et al. [16]. The residence time also affects the diffusion of reactants in the droplet and therefore changes the reactive layer thickness. Since the diffusion length is proportional to $\sqrt{t}$, the reactive layer thickness was scaled by the square root of the residence time relative to that for 1 slm. The values for the reactive layer thickness are also listed in Table 5.

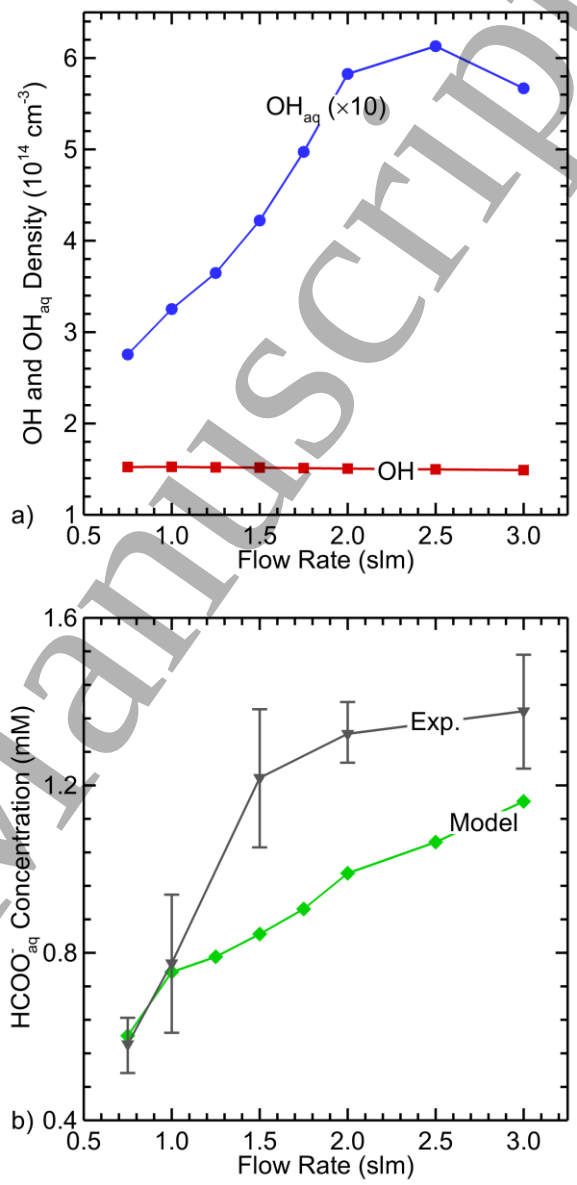

Figure 6. Plasma properties as a function of gas flow rates. a) OH and OH_{aq} densities as the power begins to ramp down (droplet exciting the plasma) and b) $HCOO^-_{aq}$ concentration at the time of collection compared to experimental measurements from Nayak et al. [16]. Aqueous quantities are averaged over the droplet.

The OH density as the power begins to ramp down (droplet exiting the plasma) is shown in Figure 6a. Note that this time varies depending on the flow rate. The gas phase OH density does not depend on flow rate. As shown in Figure 3b, the density of OH reaches a near steady state after 2 ms. This steady state value will

not depend on flow rate or residence time unless the water density is depleted.

The OH_{aq} density averaged over the droplet as the power begins to ramp down is shown in Figure 6a, and the $HCOO^-_{aq}$ concentration at the residence time plus 10 ms averaged over the droplet is shown in Figure 6b. These aqueous densities are averaged over the droplet as described by Eq. 1. The OH_{aq} density increases from 0.75 slm to 2.5 slm. At 0.75 slm (13.5 ms residence time), the OH_{aq} density reaches a maximum near 6.8 ms. However, at 0.75 slm, the maximum occurs 6.8 ms before the power begins to ramp down (end of the plasma channel), and the density of OH_{aq} decreases due to consumption by $O_2^-{}_{aq}$. At 1 slm, the maximum in OH_{aq} density occurs 3.7 ms before the power ramps down, and so the decrease in the density OH_{aq} due to competing reactions is less in the remaining 3.7 ms. As the flow rate continues increasing to 2 slm, the maximum in OH_{aq} occurs closer to when the power ramps down. At 2.5 slm, the maximum in OH_{aq} density occurs just as the power begins to ramp down, and so the density of OH_{aq} does not decrease.

The droplet averaged $HCOO^-_{aq}$ concentration increases from 0.75 slm to 2.5 slm. This increase in $HCOO^-_{aq}$ concentration is due to the decrease in the reactive layer thickness and decrease in residence time. The OH_{aq} has less $HCOO^-_{aq}$ to interact with as the reactive layer thickness decreases, which increases the remaining inventory when averaged over the entire droplet. The OH_{aq} also has less time to interact with the $HCOO^-_{aq}$ in the reactive layer, leading to a small increase in $HCOO^-_{aq}$ density. As the flow rate increases beyond 2.5 slm (residence time decreases below 5.7 ms), the OH_{aq} density decreases and $HCOO^-_{aq}$ density increases. As the residence time decreases, the $HCOO^-_{aq}$ density in the reactive layer increases both as a result of there being less time for the OH_{aq} to react with $HCOO^-_{aq}$ as well as the decrease in reactive layer thickness. Therefore, OH_{aq} density decreases, as it is consumed in the reaction with $HCOO^-_{aq}$, and, to a lesser extent, $O_2^-{}_{aq}$.

The measured $HCOO^-_{aq}$ concentrations are also shown in Figure 6b, increasing as flow rate increases. The $HCOO^-_{aq}$ concentrations predicted by the model follow the same trend. At low flow rates (< 1.5 slm), the $HCOO^-_{aq}$ in the reactive layer is depleted to less than 5% of its initial value. However, the decrease in the reactive layer thickness with increasing flow rate (smaller residence time) means less $HCOO^-_{aq}$ in the droplet is in the reactive layer and available to react with OH_{aq}. In the experiments, $HCOO^-_{aq}$ at the surface of the droplet is depleted but may be replenished by diffusion from the interior of the droplet. At lower flow rates (longer residence

times), $HCOO^-_{aq}$ has more time to diffuse from the center of the droplet to the surface, resulting in more $HCOO^-_{aq}$ being consumed. While this process is not directly included in the model, the change in reactive layer thickness with flow rate approximates this process.

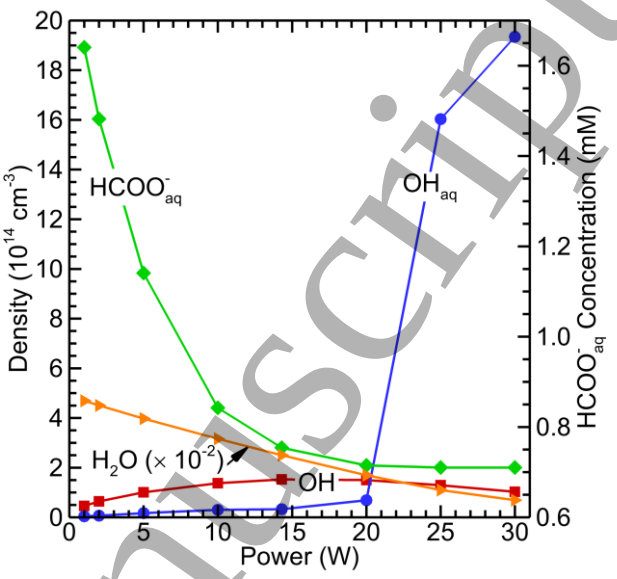

Figure 7. OH, H_2O, and OH_{aq} densities as the power begins to ramp down (10.1 ms exiting the plasma channel) and $HCOO^-_{aq}$ concentration at the time of collection as a function of power. Aqueous quantities are averaged over the droplet.

D. Power Deposition

Power deposition in the He/H_2O plasma was increased and decreased from the base case of 14.3 W. As the power deposition increases, the electron density increases, leading to more electron-impact collisions and more reactive chemistry. The OH and H_2O densities in the gas phase are shown in Figure 7 as the power begins to ramp down (10.1 ms). At low power (< 14.3 W), the OH density increases as the power increases as the steady-state electron density increases while the density of H_2O is not significantly depleted. Therefore, the rate of electron-impact dissociation of H_2O, the dominant source of OH, increases. However, as power increases beyond 14.3 W, the OH density decreases in spite of the steady-state electron density increasing. This decrease in OH density is due to the depletion of H_2O in the gas phase by electron-impact reactions, as shown in Figure 7. With H_2O being the primary precursor to OH, the depletion of H_2O leads to a reduction in OH density.

The OH_{aq} density as the power begins to ramp down (10.1 ms) and the $HCOO^-_{aq}$ concentration after an additional 10 ms (time of collection) are also shown in Figure 7, both averaged over the droplet as described in Eq. 1. Below 10 W, the $HCOO^-_{aq}$ concentration decreases as power increases as expected. As the $HCOO^-_{aq}$ concentration decreases, the OH_{aq} concentration increases because the consumption of OH_{aq} by reaction with $HCOO^-_{aq}$ decreases. As the power increases above 10 W, the decrease in $HCOO^-_{aq}$ slows because a substantial amount of $O_2^-{}_{aq}$ has been produced to consume OH_{aq} at rates larger than the reaction with $HCOO^-_{aq}$. As the power increases above 25 W, the $HCOO^-_{aq}$ concentration remains constant. This is because the $HCOO^-$

$_{aq}$ in the reactive layer is almost completely consumed, and the droplet-averaged density of $HCOO^-_{aq}$ is determined by the initial concentration in the core. When including diffusion from the core to the reactive layer, we expect that there will be some increasing consumption of the droplet-averaged $HCOO^-_{aq}$. At 25 W, the OH_{aq} density increases significantly. While OH_{aq} is consumed by reactions with $O_2^-{}_{aq}$ after the density of $HCOO^-_{aq}$ decreases, OH_{aq} increases once $O_2^-{}_{aq}$ is consumed due to solvation of OH.

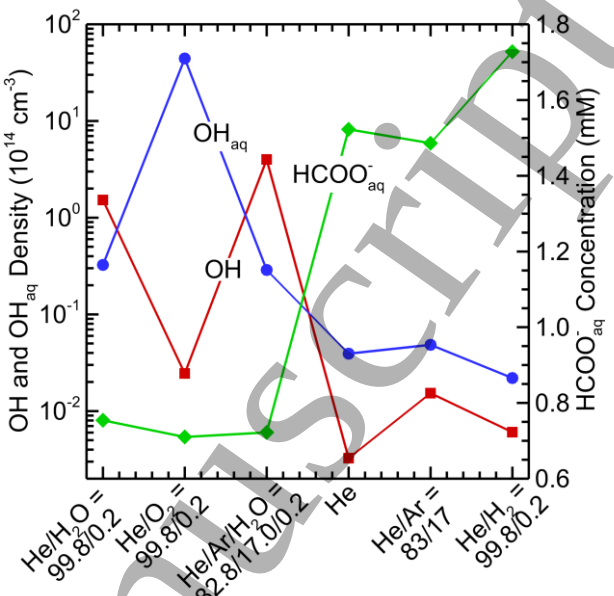

Figure 8. OH and OH_{aq} densities as the power begins to ramp down (10.1 ms, when the droplet exits the plasma) and $HCOO^-_{aq}$ concentration at the time of collection for different gas mixtures at 1 slm. Aqueous quantities are averaged over the droplet.

Experimentally, increasing the power at the same gas flow rate will likely increase the droplet evaporation rate and reduce the droplet diameter. The smaller size of the droplet will lead to rapid diffusion of $HCOO^-_{aq}$ from the nonreactive core to the reactive layer, leading to increased consumption of $HCOO^-_{aq}$ by OH_{aq}.

E. Gas Mixtures

When the plasma is sustained in different gas mixtures, different reaction pathways and possible radical species are formed in the plasma. For example, in plasmas with high concentrations of O_2, O and O_3 are the dominant reactive species; while in plasmas with high concentrations of H_2O, OH is the dominant radical reactive species. The degradation of $HCOO^-_{aq}$ has been investigated for different gas mixtures [13–16], including He with admixtures of H_2O, O_2, Ar, and Ar/H_2O. The gas mixtures examined in this section have the same level of impurities as previously measured for pure He (2.3 ppm H_2O, 1.5 ppm O_2, and 6.0 ppm N_2) [14]. The power deposition varies for each gas mixture examined and is shown in Table 6.

The OH density as the power begins to ramp down (10.1 ms) for different gas mixtures is shown in Figure 8. The He/H_2O = 99.8/0.2 and He/Ar/H_2O = 82.8/17.0/0.2 mixtures have the highest density of OH in the gas phase since the main formation mechanism of OH is electron-impact dissociation of H_2O. While H_2O can be found in the gas phase due to impurities and

evaporation of the droplet, the main source of H_2O is in the initial gas mixture and flow. The He/O_2 = 99.8/0.2 mixture has the next highest density of OH in the gas phase due to reactions of HO_2 and O. The other three gas mixtures (He, He/Ar = 83/17, and He/H_2 = 99.8/0.2) have OH densities nearly two orders of magnitude lower than the OH densities in the He/H_2O and $He/Ar/H_2O$ mixtures.

The OH_{aq} density as the power begins to ramp down (10.1 ms) and $HCOO^-_{aq}$ concentration at the time of collection are also shown in Figure 8, both averaged over the droplet. Where OH density was high in the gas phase, OH_{aq} density is also relatively high, since solvation of OH from the gas is its dominant source. However, since OH_{aq} is consumed by $O_2^-{}_{aq}$, the density of OH_{aq} is lower than the density of OH. In the He/O_2 mixture, the OH density is relatively low, and the OH_{aq} density is the highest of all gas mixtures examined. In this case, OH_{aq} is formed not in the gas phase, but in the liquid phase by $O_{aq} + H_2O_{aq} \rightarrow OH_{aq} + OH_{aq}$ [17]. Since the He/O_2 mixture has an abundance of O to solvate into the droplet, OH_{aq} is readily formed within the droplet. Therefore, the decomposition of $HCOO^-_{aq}$ is due to the OH_{aq} formed by O_{aq} instead of by solvation of gas phase OH. However, this value for OH_{aq} may be sensitive to the Henry's law constant of O. With the He/O_2 mixture, the rate of OH_{aq} production by O_{aq} is higher than the consumption of OH_{aq} by $O_2^-{}_{aq}$, and OH_{aq} does not significantly decrease over the power on period. For the He/H_2O, He/O_2, and $He/Ar/H_2O$ mixtures, the density $HCOO^-_{aq}$ in the reactive layer is depleted to below 4% of the initial $HCOO^-_{aq}$ concentration, leading to a relatively constant $HCOO^-_{aq}$ concentration (averaged over the droplet).

For the He, He/Ar, and He/H_2 mixtures, the $HCOO^-_{aq}$ is decreased by less than 0.5 mM from its initial concentration of 2 mM. In the He and He/Ar mixtures, OH_{aq} is formed both by solvation of gas phase OH as well as $O_{aq} + H_2O_{aq} \rightarrow OH_{aq} + OH_{aq}$. The rate of OH_{aq} formation by UV/VUV radiation is at least 4 orders of magnitude lower than the rate of formation by $O_{aq} + H_2O_{aq}$ in the He mixture and nearly 3 orders of magnitude lower in the He/Ar mixture. The total density of the radiating states is below 2×10^9 cm^{-3} in the He mixture and below 5×10^{11} cm^{-3} in the He/Ar mixture due to their being quenched by H_2O and impurities. Without the UV/VUV radiation, $HCOO^-_{aq}$ increases by less than 0.02 mM across all gas mixtures, with the largest difference in the He/Ar mixture. Therefore, in this system, UV/VUV radiation does not play a large role in OH_{aq} production and $HCOO^-_{aq}$ degradation. In the He/H_2 mixture, the H density is 3 orders of magnitude larger than the OH density. However, H has a low Henry's law coefficient

(6.48×10^{-3}) compared to OH (620), leading to H_{aq} only being a factor of 1.7 larger than OH_{aq}. While H_{aq} has a higher density than OH_{aq}, the rate coefficient of H_{aq} reacting with $HCOO^-_{aq}$ is an order of magnitude lower than that of OH_{aq} reacting with $HCOO^-_{aq}$. Therefore, $HCOO^-_{aq}$ is still consumed primarily through OH_{aq}. Since OH_{aq} is not abundant, $HCOO^-_{aq}$ is not depleted.

The results from the model are compared to the experimental measurements in Table 9. As discussed in Section III.B, in the He/H_2O plasma, the model underpredicts the OH density by a factor of two while matching the $HCOO^-_{aq}$ density. For the He/O_2 plasma, the OH density was not measured, but the model predicts a density of 2.4×10^{12} cm^{-3}, almost two orders of magnitude lower than the He/H_2O plasma. The $HCOO^-_{aq}$ concentration matches within uncertainty, as the measurements show 0.80 mM and the model predicts 0.71 mM. For the $He/Ar/H_2O$ plasma, the model underpredicts the OH density by 20%. The $HCOO^-_{aq}$ concentration again matches within uncertainty, as the model predicts 0.79 mM and the experiments show 0.72 mM.

Species in addition to OH_{aq} and H_{aq} could also play a role in $HCOO^-_{aq}$ depletion. In Nayak et al., it was argued based on the work of Jirasek and Lukes [26] that O_{aq} could directly interact with $HCOO^-_{aq}$ [16]. UV/VUV photodissociation and photoionization of H_2O_{aq} was shown to not play a large role in OH_{aq} production and subsequent $HCOO^-_{aq}$ degradation due to the low density of radiating states. However, in other systems with larger densities of radiating states, UV/VUV photodissociation could play an important role, particularly when large amounts of OH are not produced in the gas phase. Additionally, photodetachment of electrons from negative ions (OH^-_{aq}, $HCOO^-_{aq}$) may be important. As electron affinities of typical negative ions are on the order of 1 eV, most radiation is energetically able to produce photodetachment. In this system, photodetachment could increase OH_{aq} through detachment from OH^-_{aq} or degrade $HCOO^-_{aq}$ directly.

F. Water Percentage

While different gas mixtures produce varying levels of OH and OH_{aq}, varying H_2O percentage in the He/H_2O mixture can also change the OH and OH_{aq} levels, allowing the OH density to be tuned to the desired amount. Note that to compare with experiments, the results in this section are with a flow rate of 1.5 slm, compared to 1 slm in previous sections. As discussed in Section IV.C., the flow rate changes the reactive layer thickness due to the shorter (or longer) time for transport of solvating species into the droplet. Therefore, the reactive layer thickness is decreased to 5.5 μm to match that at 1.5 slm.

The OH density as the power begins to ramp down (8.4 ms. exit of the plasma channel) is shown in Figure 9a at a flow rate of 1.5 slm. As the H_2O percentage in the initial gas mixture increases, the OH density increases because electron-impact dissociation of H_2O is the main production mechanism of OH. The predicted densities of OH density are lower than experimental measurements by about 25%, but the trends in OH density are the same between the measurements and model results.

The OH_{aq} density as the power begins to ramp down (8.4 ms, exit of plasma channel) is shown in Figure 9a, and the $HCOO^-_{aq}$ concentration at the time of collection is shown in Figure 9b. Both the OH_{aq} density and $HCOO^-_{aq}$ density are averaged over the droplet as described in Eq. 1. At low H_2O percentages (< 0.1%), the $HCOO^-_{aq}$ concentration continually decreases as the $HCOO^-_{aq}$ density in the reactive layer is decreasing. As the $HCOO^-_{aq}$ density decreases, the OH_{aq} density increases as the consumption of OH_{aq} by $HCOO^-_{aq}$ decreases. The $O_2^-{}_{aq}$ density is low, and $O_2^-{}_{aq}$ does not consume a large proportion of OH_{aq} compared to reactions with $HCOO^-_{aq}$. At 0.2% H_2O, the density of OH_{aq} reaches a maximum at 6.3 ms, as $O_2^-{}_{aq}$ begins consuming more OH_{aq} than $HCOO^-_{aq}$ later in the power on period. Beyond 0.2% H_2O,

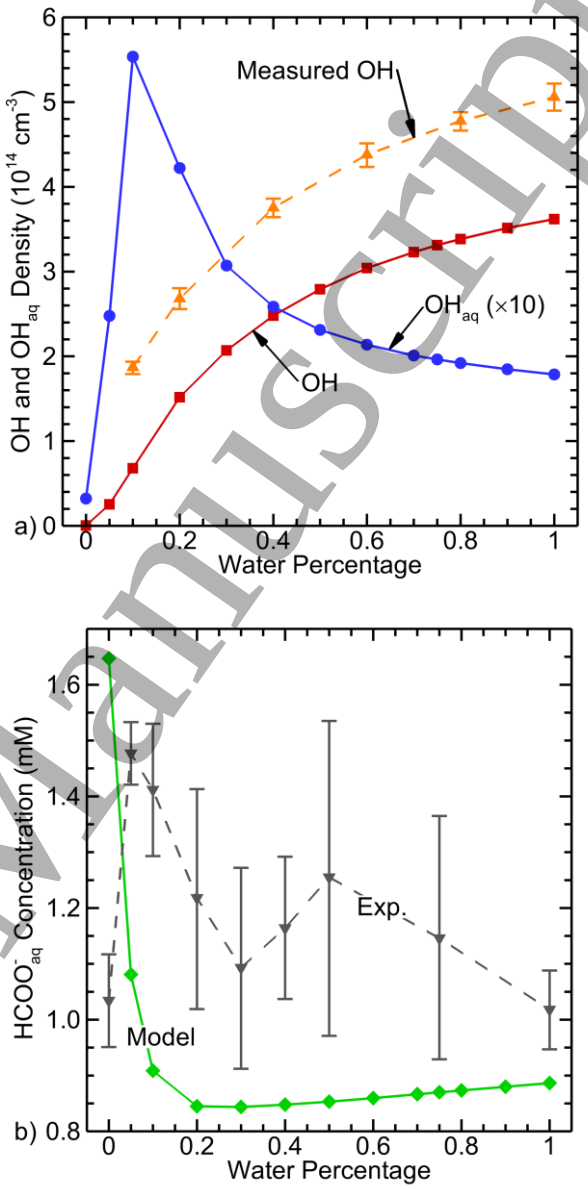

Figure 9. Droplet properties as a function of percentage of water in the inlet flow (He + X% H_2O). a) OH and OH_{aq} densities as the power begins to ramp down (8.4 ms, at exit of droplet from the plasma) at 1.5 slm compared to experimental measurements of OH from Oinuma et al. [15]. b) $HCOO^-_{aq}$ concentration at the time of collection compared to experimental measurements from Oinuma et al. [15]. Aqueous quantities are averaged over the droplet.

the $HCOO^-_{aq}$ concentration increases slightly as $O_2^-_{aq}$ begins consuming more OH_{aq} earlier in the power on period, lessening the ability of OH_{aq} to consume more $HCOO^-_{aq}$. However, the increase in $HCOO^-_{aq}$ concentration is less than 0.05 mM from 0.2% H_2O to 1% H_2O. This is consistent with a transition from a $HCOO^-_{aq}$ decomposition limited by gas phase OH flux towards the droplet, to a decomposition limited by liquid phase transport of $HCOO^-_{aq}$ as discussed in Nayak et al. [16].

The OH_{aq} density increases up to 0.1% H_2O. However, at larger H_2O percentages, OH_{aq} at the exit of the plasma channel begins to decrease. As the H_2O percentage increases, $HCOO^-_{aq}$ decreases earlier in the power on period. Therefore, $O_2^-_{aq}$, a byproduct of $HCOO^-_{aq}$ degradation, also increases earlier in the power on period and becomes the dominant consumption mechanism of OH_{aq} earlier in the power on period when the $O_2^-_{aq}$ density is around 33% of the $HCOO^-_{aq}$ density. Due to the abundance of $O_2^-_{aq}$ at earlier times with increasing H_2O percentage, $O_2^-_{aq}$ has more time to consume OH_{aq}, decreasing its density at larger H_2O percentages.

The measured $HCOO^-_{aq}$ concentrations are also shown in Figure 9b. At 0% H_2O (pure He), the experiments show a high level of $HCOO^-_{aq}$ degradation, while the model does not predict this. This mismatch could indicate that there are other reactive species besides OH_{aq} and H_{aq} that consume $HCOO^-_{aq}$. These other reactive species could be excited states of He that are quenched entering the droplet. However, the majority of those states will be quenched by reactions with H_2O_{aq} (included in the model) and not directly with $HCOO^-_{aq}$. From 0.05% H_2O to 0.3% H_2O, the measured $HCOO^-_{aq}$ concentration decreases. This trend is predicted by the model up to 0.2% H_2O. After 0.3% H_2O, the measured $HCOO^-_{aq}$ concentration remains relatively constant, matching the predictions by the model. However, the model predicts a concentration of 0.84 mM to 0.88 mM, while the measurements show a concentration near 1.1 mM. This discrepancy is likely due to the thickness of the reactive layer at 5.5 μm. The reactive layer thickness was initially chosen to match the experimental measurements at 1 slm (residence time of 10 ms) and scaled for the flow rate of 1.5 slm. While this scaling reproduces the trends as seen in Section IV.C, this mode of scaling may not be applicable to all flow rates.

V. Concluding Remarks

The degradation of $HCOO^-_{aq}$, a model organic compound, by OH_{aq} from plasma-produced OH was computationally investigated in an atmospheric pressure RF discharge sustained in He/H_2O mixtures using a 0-dimensional plasma chemistry model *GlobalKin*. To best match the experimental results, the droplet was modeled as two zones: a reactive layer and a nonreactive

core. The thickness of the reactive layer was determined to be 6 μm for the base case so the model predictions of $HCOO^-_{aq}$ concentration would match the experimentally measured $HCOO^-_{aq}$ concentration at a single operating point at 1 slm. Over the 10 ms the droplet is exposed to the plasma, the OH density reaches a steady state value of 1.5×10^{14} cm^{-3}, in agreement with experiments [16]. In the droplet, $HCOO^-_{aq}$ decreases due to reactions with OH_{aq} that solvates from the gas phase into the liquid phase due to its high Henry's law constant. Initially, as the $HCOO^-_{aq}$ in the reactive layer is consumed, the density of OH_{aq} in the reactive layer increases. While the main consumption mechanism of OH_{aq} is the reaction with $HCOO^-_{aq}$ during the first portion of plasma exposure, reactions with $O_2^-{}_{aq}$, a byproduct of $HCOO^-_{aq}$ degradation, become dominant once $O_2^-{}_{aq}$ reaches 33% of $HCOO^-_{aq}$ density. The role of photodissociation by UV/VUV radiation in producing OH_{aq} in the droplet was investigated. Including photolysis by UV/VUV radiation did not significantly change $HCOO^-_{aq}$ depletion due to low densities of radiating states which are quenched by reactions with H_2O. For plasma conditions were the OH flux is less dominating in producing OH_{aq} and where excited states that emit UV/VUV photons are abundant, we expect the role of UV/VUV radiation to be more important.

The variation of droplet and plasma properties affects the amount of $HCOO^-_{aq}$ consumed in the reactive layer. While all variations examined change the species densities in the liquid, only the power deposition, gas mixture, and percentage of H_2O in the inlet changed the gas phase OH density. The droplet diameter, initial $HCOO^-_{aq}$ concentration, and gas flow rate do not significantly affect the OH density. In general, early in plasma exposure, OH_{aq} reacts primarily with $HCOO^-_{aq}$. However, later in plasma exposure, the formation of $CO_2^-{}_{aq}$ by the reaction between OH_{aq} and $HCOO^-_{aq}$ leads to the formation of $O_2^-{}_{aq}$. The increase in $O_2^-{}_{aq}$ due to $HCOO^-_{aq}$ consumption leads to a reaction between OH_{aq} and $O_2^-{}_{aq}$ becoming the dominant consumption mechanism of OH_{aq}. Then, the reactions of $O_2^-{}_{aq}$ and OH_{aq} lead to decreases in OH_{aq}.

Acknowledgements

This work was supported by the National Science Foundation (PHY-1902878, PHY 1903151 and CBET-2032604). This material was also based upon work supported by the U.S. Department of Energy, Office of Science, Office of Fusion Energy Sciences under Award No. DE-SC0020232; the Army Research Office accomplished under Grants No. W911NF-20-1-0105.

Conflict of Interest

The authors have no conflicts of interest to disclose.

Data Availability

The data that support the findings of this study are either contained within this paper or available from the corresponding author upon reasonable request.

References

[1] J. E. Foster, Phys. Plasmas **24,** 055501 (2017).

[2] P. J. Bruggeman, M. J. Kushner, B. R. Locke, J. G. E. Gardeniers, W. G. Graham, D. B. Graves, R. C. H. M. Hofman-Caris, D. Maric, J. P. Reid, E. Ceriani, D. Fernandez Rivas, J. E. Foster, S. C. Garrick, Y. Gorbanev, S. Hamaguchi, F. Iza, H. Jablonowski, E. Klimova, J. Kolb, F. Krcma, P. Lukes, Z. MacHala, I. Marinov, D. Mariotti, S. Mededovic Thagard, D. Minakata, E. C. Neyts, J. Pawlat, Z. L. Petrovic, R. Pflieger, S. Reuter, D. C. Schram, S. Schröter, M. Shiraiwa, B. Tarabová, P. A. Tsai, J. R. R. Verlet, T. Von Woedtke, K. R. Wilson, K. Yasui and G. Zvereva, Plasma Sources Sci. Technol. **25,** 053002 (2016).

[3] T. Von Woedtke, D. Weltmann, S. Emmert, H. Metelmann, S. Rupf and K.-D. Weltmann, Phys. Plasmas **27,** 070601 (2020).

[4] A. Stancampiano, T. Gallingani, M. Gherardi, Z. Machala, P. Maguire, V. Colombo, J. Pouvesle and E. Robert, Appl. Sci. **9,** 3861 (2019).

[5] M. E. Hassan, M. Janda and Z. Machala, Water **13,** 182 (2021).

[6] Z. Liu, S. Wang, B. Pang, H. Zhang, Y. Gao, D. Xu and M. G. Kong, J. Phys. D. Appl. Phys. **54,** 215203 (2021).

[7] R. K. Singh, E. Brown, S. Mededovic Thagard and T. M. Holsen, J. Hazard. Mater. **408,** 124452 (2021).

[8] J. Jose and L. Philip, J. Environ. Manage. **286,** 112202 (2021).

[9] S. Jaiswal and E. M. Aguirre, AIP Adv. **11,** 045311 (2021).

[10] E. Casado, M. C. Garcia, D. A. Krawczyk, F. J. Romero-Salguero and A. Rodero, Plasma Process. Polym. **17,** 2000030 (2020).

[11] I. Sremački, G. Bruno, H. Jablonowski, C. Leys, A. Nikiforov and K. Wende, Plasma Sources Sci. Technol. **30,** 095018 (2021).

[12] T. Xia, A. Kleinheksel, E. M. Lee, Z. Qiao, K. R. Wigginton and H. L. Clack, J. Phys. D. Appl. Phys. **52,** 255201 (2019).

[13] G. Nayak, M. S. Simeni, J. Rosato, N. Sadeghi and P. J. Bruggeman, J. Appl. Phys. **128,** 243302 (2020).

[14] G. Nayak, N. Sadeghi and P. J. Bruggeman, Plasma Sources Sci. Technol. **28,** 125006 (2019).

[15] G. Oinuma, G. Nayak, Y. Du and P. J. Bruggeman, Plasma Sci. Technol. **29,** 095002 (2020).

[16] G. Nayak, G. Oinuma, Y. Yue, J. S. Sousa and P. J. Bruggeman, Plasma Sources Sci. Technol. **30,** 115003 (2021).

[17] A. M. Lietz and M. J. Kushner, J. Phys. D. Appl. Phys. **49,** 425204 (2016).

[18] W. Van Gaens and A. Bogaerts, J. Phys. D. Appl. Phys. **46,** 275201 (2014).

[19] S. Norberg, (University of Michigan, 2015).

[20] F. Emmert, H. H. Angermann, R. Dux and H. Langhoff, J. Phys. D. Appl. Phys. **21,** 667 (1988).

[21] P. Tian and M. J. Kushner, Plasma Sources Sci. Technol. **24,** 34017 (2015).

[22] W. Tian and M. J. Kushner, J. Phys. D. Appl. Phys. **47,** 165201 (2014).

[23] W. Tian, K. Tachibana and M. J. Kushner, J. Phys. D. Appl. Phys. **47,** 055202 (2014).

[24] R. Sander, Atmos. Chem. Phys. **15,** 4399 (2015).

[25] M. U. Sander, K. Luther and J. Troe, Berichte der Bunsengesellschaft für Phys. Chemie **97,** 953 (1993).

[26] V. Jirásek and P. Lukeš, J. Phys. D. Appl. Phys. **53,** 505206 (2020).

[27] G. Imoberdorf and M. Mohseni, Chem. Eng. Sci. **66,** 1159 (2011).

[28] Y. Zheng, L. Wang and P. Bruggeman, J. Vac. Sci. Technol. A **38,** 063005 (2020).

[29] T. Løgager and K. Sehested, J. Phys. Chem. **97,** 10047 (1993).

[30] M. Meyer, G. Nayak, P. J. Bruggeman and M. J. Kushner, "Sheath Formation around a Dielectric Droplet in a He Atmospheric Pressure Plasma", J. Appl. Phys. 132, 083303 (2022).

Table 1. Species included in the reaction mechanism.

Charged Species in the Gas Phase	e, He^+, He_2^+, HeH^+, Ar^+, Ar_2^+, ArH^+ H^+, H^-, H_2^+, H_3^+, OH^+, OH^-, H_2O^+, H_3O^+ O_2^+, O_2^-, O_4^+, O^+, O^-, O_3^-, N_2^+, N_3^+, N_4^+, N^+ NO^+, NO_2^+, NO_2^-, NO_3^-, $NO^+(H_2O)$, $NO^+(H_2O)_2$, $NO^+(H_2O)_3$, $N^+(H_2O)$, $NO^+(O_2)$ $H_2O^+(H_2O)$, $O_2^+(H_2O)$, $H_3O^+(H_2O)$, $H_3O^+(H_2O)_2$, $H_3O^+(H_2O)_3$, $H_3O^+(H_2O)_4$, $H_3O^+(H_2O)_5$, $H_3O^+(H_2O)_6$, $O_2^-(H_2O)$, $O_2^-(H_2O)_2$, $O^-(H_2O)$, $OH^-(H_2O)$, $OH^-(H_2O)_2$ CO^+, CO_2^+
Neutral Species in the Gas Phase	He, Ar H, H_2, OH, H_2O, HO_2, H_2O_2 O_2, O, O_3, N_2, N NO, NO_2, NO_3, N_2O, N_2O_3, N_2O_4, N_2O_5, NH, HNO, HNO_2, HNO_3, HNO_4 CO, CO_2, HCOOH, HCOO
Excited States in the Gas Phase	$He(2^3S)$, $He(2^1S)$, $He(2^3P)$, $He(2^1P)$, He(3P), He(3S), He_2^*, $Ar(1s_1)$, $Ar(1s_2)$, $Ar(1s_3)$, $Ar(1s_4)$, Ar(4P), Ar(4D), Ar_2^* H^*, $H_2(r)$, $H_2(v)$, H_2^*, $OH(A^2\Sigma)$, $H_2O(v)$ $O_2(v)$, $O_2(r)$, $O_2(^1\Delta)$, $O_2(^1\Sigma)$, $O(^1D)$, O_3^*, $N_2(r)$, $N_2(v)$, $N_2(A^3\Sigma_u)$, $N_2(a'^1\Sigma)$, $N(^2D)$ $N_2O(v)$ $CO(v)$, $CO_2(v)$
Charged Species Only Present in the Liquid Phase	$e(H_2O)_{aq}$, $HO_2^-{}_{aq}$, $ONOO^-{}_{aq}$, $NO_4^-{}_{aq}$, $Na^+{}_{aq}$, $HCOO^-{}_{aq}$, $CO_2^-{}_{aq}$, $NO_3^{-2}{}_{aq}$, $HNO_3^-{}_{aq}$
Neutral Species Only Present in the Liquid Phase	$ONOOH_{aq}$, $NaOH_{aq}$

Table 2. Aqueous reaction mechanism additions or changes from Ref. [17]**.**

Reaction	Rate Coefficient (cm^3/s unless otherwise specified)	Note
$H_2O_{aq} + H_2O_{aq} \rightarrow H_3O^+_{aq} + OH^-_{aq}$	1.83×10^{-28}	Ref. [15][2]
$H_3O^+_{aq} + OH^-_{aq} \rightarrow H_2O_{aq} + H_2O_{aq}$	4.98×10^{-11}	Ref. [15][2]
Ion and excited state solvation		
$e_{aq} + H_2O_{aq} \rightarrow e(H_2O)_{aq}$	5×10^{-9}	20 fs solvation time[2]
$H_3^+{}_{aq} + H_2O_{aq} \rightarrow H_3O^+_{aq} + H_{2aq}$	5×10^{-15}	[1,3]
$N^+(H_2O)_{aq} + H_2O_{aq} \rightarrow H_2O^+_{aq} + N_{aq} + H_2O_{aq}$	5×10^{-15}	[1,3]
$OH^+_{aq} + H_2O_{aq} \rightarrow H_2O^+_{aq} + OH_{aq}$	5×10^{-15}	[1,3]
$Ar^+_{aq} + H_2O_{aq} \rightarrow H_2O^+_{aq} + Ar_{aq}$	5×10^{-15}	[1,3]
$Ar^+_{2aq} + H_2O_{aq} \rightarrow H_2O^+_{aq} + Ar_{aq} + Ar_{aq}$	5×10^{-15}	[1,3]
$ArH^+_{aq} + H_2O_{aq} \rightarrow H_3O^+_{aq} + Ar_{aq}$	5×10^{-15}	[1,3]
$H^-_{aq} + H_2O_{aq} \rightarrow H_{2aq} + OH^-_{aq}$	5×10^{-15}	[1,3]
$N_2(r)_{aq} + H_2O_{aq} \rightarrow H_2O_{aq} + N_{2aq}$	5×10^{-15}	[1,3]
$H^*_{aq} + H_2O_{aq} \rightarrow H_{aq} + OH_{aq} + H_{aq}$	5×10^{-15}	[1,3]
$H_2O(v)_{aq} + H_2O_{aq} \rightarrow H_2O_{aq} + H_2O_{aq}$	5×10^{-15}	[1,3]
$N(^2D)_{aq} + H_2O_{aq} \rightarrow NH_{aq} + OH_{aq}$	6.93×10^{-39}	Based on T_{liquid} = 300 K[2]
$OH(A^2\Sigma)_{aq} + H_2O_{aq} \rightarrow OH_{aq} + H_{aq} + OH_{aq}$	5×10^{-15}	[1,3]
$H_2(r)_{aq} + H_2O_{aq} \rightarrow H_{2aq} + H_2O_{aq}$	5×10^{-15}	[1,3]
$H_2(v)_{aq} + H_2O_{aq} \rightarrow H_{2aq} + H_2O_{aq}$	5×10^{-15}	[1,3]
$H^*_{2aq} + H_2O_{aq} \rightarrow H_{2aq} + H_{aq} + OH_{aq}$	5×10^{-15}	[1,3]
$O_2(r)_{aq} + H_2O_{aq} \rightarrow O_{2aq} + H_2O_{aq}$	5×10^{-15}	[1,3]
$O_3^*{}_{aq} + H_2O_{aq} \rightarrow O_{3aq} + H_2O_{aq}$	5×10^{-15}	[1,3]
$O_2(^1\Delta)_{aq} + H_2O_{aq} \rightarrow O_{2aq} + H_2O_{aq}$	7.7×10^{-18}	Ref. [18], Based on T_{liquid} = 300 K[2]

$OH(A^2\Sigma)_{aq} + H_2O_{aq} \rightarrow OH_{aq} + H_2O_{aq}$	1.2×10^{-11}	[1,3]
$N_2O(v)_{aq} + H_2O_{aq} \rightarrow N_2O_{aq} + H_2O_{aq}$	5×10^{-15}	[1,3]
<u>Ar excited state solvation</u>		
$M_{aq} + H_2O_{aq} \rightarrow H_{aq} + OH_{aq} + Ar_{aq}$ M = $Ar(1s_1)_{aq}$, $Ar(1s_2)_{aq}$, $Ar(1s_3)_{aq}$, $Ar(1s_4)_{aq}$, $Ar(4P)_{aq}$, $Ar(4D)_{aq}$	5×10^{-15}	[1,3]
$Ar_2^*{}_{aq} + H_2O_{aq} \rightarrow H_{aq} + OH_{aq} + Ar_{aq} + Ar_{aq}$	5×10^{-15}	[1,3]
$M_{aq} + O_{2aq} \rightarrow O(^1D)_{aq} + O_{aq} + Ar_{aq}$ M = $Ar(1s_1)_{aq}$, $Ar(1s_2)_{aq}$, $Ar(1s_3)_{aq}$, $Ar(1s_4)_{aq}$, $Ar(4P)_{aq}$, $Ar(4D)_{aq}$	5×10^{-15}	[1,3]
$Ar^*{}_{2aq} + O_{2aq} \rightarrow O(^1D)_{aq} + O_{aq} + Ar_{aq} + Ar_{aq}$	5×10^{-15}	[1,3]
$M_{aq} + O_{3aq} \rightarrow O(^1D)_{aq} + O_{2aq} + Ar_{aq}$ M = $Ar(1s_1)_{aq}$, $Ar(1s_2)_{aq}$, $Ar(1s_3)_{aq}$, $Ar(1s_4)_{aq}$, $Ar(4P)_{aq}$, $Ar(4D)_{aq}$	5×10^{-15}	[1,3]
$Ar_2^*{}_{aq} + O_{3aq} \rightarrow O(^1D)_{aq} + O_{2aq} + Ar_{aq} + Ar_{aq}$	5×10^{-15}	[1,3]
$M_{aq} + H_2O_{2aq} \rightarrow OH_{aq} + OH_{aq} + Ar_{aq}$ M = $Ar(1s_1)_{aq}$, $Ar(1s_2)_{aq}$, $Ar(1s_3)_{aq}$, $Ar(1s_4)_{aq}$, $Ar(4P)_{aq}$, $Ar(4D)_{aq}$	5×10^{-15}	[1,3]
$Ar_2^*{}_{aq} + H_2O_{2aq} \rightarrow OH_{aq} + OH_{aq} + Ar_{aq} + Ar_{aq}$	5×10^{-15}	[1,3]
<u>Reactive oxygen species</u>		
$e(H_2O)_{aq} + H_2O_{aq} \rightarrow e_{aq} + H_2O_{aq} + H_2O_{aq}$	1×10^{-13}	[1,3]
$e(H_2O)_{aq} + Ar_{aq} \rightarrow e_{aq} + H_2O_{aq} + Ar_{aq}$	1×10^{-13}	[1,3]
$e(H_2O)_{aq} + H_2O_{aq} \rightarrow H_{aq} + OH^-{}_{aq} + H_2O_{aq}$	3×10^{-20}	[1]
$e(H_2O)_{aq} + H_2O^+{}_{aq} \rightarrow H_{aq} + OH_{aq} +$	1×10^{-9}	[1]

H_2O_{aq}		
$H_2O^+_{aq} + H_2O_{aq} \rightarrow H_3O^+_{aq} + OH_{aq}$	1×10^{-17}	[1]
$H_3O^+_{aq} + O^-_{aq} \rightarrow OH_{aq} + H_2O_{aq}$	1.66×10^{-11}	Ref. [15][1]
$H_3O^+_{aq} + O_2^-{}_{aq} \rightarrow HO_{2aq} + H_2O_{aq}$	9.46×10^{-11}	Ref. [15][1]
$OH_{aq} + OH_{aq} \rightarrow H_2O_{2aq}$	1.66×10^{-12}	Ref. [15][2]
$OH_{aq} + HO_{2aq} \rightarrow O_{2aq} + H_2O_{aq}$	1.66×10^{-11}	Ref. [15][2]
$OH_{aq} + H_2O_{2aq} \rightarrow HO_{2aq} + H_2O_{aq}$	5.84×10^{-14}	Ref. [15][2]
$OH_{aq} + OH^-_{aq} \rightarrow O^-_{aq} + H_2O_{aq}$	1.99×10^{-11}	Ref. [15][2]
$OH_{aq} + O^-_{aq} \rightarrow HO^-_{2aq}$	4.48×10^{-11}	Ref. [15][2]
$OH_{aq} + HO_2^-{}_{aq} \rightarrow HO_{2aq} + OH^-_{aq}$	1.25×10^{-11}	Ref. [15][2]
$O^-_{aq} + H_2O_{aq} \rightarrow OH^-_{aq} + OH_{aq}$	2.99×10^{-15}	Ref. [15][1]
$O^-_{aq} + O_{2aq} \rightarrow O_3^-{}_{aq}$	5.81×10^{-12}	Ref. [15][2]
$O^-_{aq} + H_2O_{2aq} \rightarrow O_2^-{}_{aq} + H_2O_{aq}$	8.3×10^{-13}	Ref. [15][2]
$O^-_{aq} + HO_2^-{}_{aq} \rightarrow O_2^-{}_{aq} + OH^-_{aq}$	6.64×10^{-13}	Ref. [15][2]
$O_3^-{}_{aq} + O^-_{aq} \rightarrow O_2^-{}_{aq} + O_2^-{}_{aq}$	1.16×10^{-11}	Ref. [15][2]
$O_3^-{}_{aq} \rightarrow O_{2aq} + O^-_{aq}$	4.3×10^3 1/s	Ref. [15][2]
$O_2^-{}_{aq} + H_2O_{2aq} \rightarrow O_{2aq} + OH_{aq} + OH^-_{aq}$	2.66×10^{-20}	Ref. [15][2]
$HO_{2aq} + H_2O_{aq} \rightarrow H_3O^+_{aq} + O_2^-{}_{aq}$	3.33×10^{-17}	Ref. [15][2]
$H_2O_{2aq} + HO_{2aq} \rightarrow OH_{aq} + O_{2aq} + H_2O_{aq}$	8.8×10^{-19}	Ref. [27][1]
$HO_{2aq} + HO_{2aq} \rightarrow H_2O_{2aq} + O_{2aq}$	3.32×10^{-15}	Ref. [15][1]
$HO_{2aq} + O_2^-{}_{aq} \rightarrow O_{2aq} + HO_2^-{}_{aq}$	8.3×10^{-14}	Ref. [15][1]
$e(H_2O)_{aq} + H_3O^+_{aq} \rightarrow H_{aq} + H_2O_{aq} + H_2O_{aq}$	3.82×10^{-11}	Ref. [27][1]
$H_{aq} + O_2^-{}_{aq} \rightarrow HO_2^-{}_{aq}$	3.32×10^{-11}	Ref. [27][1]
$HO_2^-{}_{aq} + O_3^-{}_{aq} \rightarrow OH^-_{aq} + O_{2aq} + O_2^-{}_{aq}$	1.48×10^{-15}	Ref. [15][1]
$HO_2^-{}_{aq} + H_2O_{aq} \rightarrow H_2O_{2aq} + OH^-_{aq}$	1.83×10^{-15}	Ref. [15][1]
$OH^-_{aq} + HO_{2aq} \rightarrow O_2^-{}_{aq} + H_2O_{aq}$	1.66×10^{-11}	Ref. [15][1]
$H_2O_{2aq} + OH^-_{aq} \rightarrow HO_2^-{}_{aq} + H_2O_{aq}$	1.66×10^{-11}	Ref. [15][1]
$H_2O_{2aq} + O_3^-{}_{aq} \rightarrow O_{2aq} + O_2^-{}_{aq} + H_2O_{aq}$	2.66×10^{-15}	Ref. [15][1]

$OH_{aq} + HO_2^-{}_{aq} \rightarrow H_2O_{aq} + O_2^-{}_{aq}$	1.16×10^{-11}	Ref. [15][1]
$O^-{}_{aq} + O_2^-{}_{aq} + H_2O_{aq} \rightarrow OH^-{}_{aq} + OH^-{}_{aq} + O_{2aq}$	3.32×10^{-35} cm^6/s	Ref. [15][1]
$O^-{}_{aq} + O^-{}_{aq} + H_2O_{aq} \rightarrow OH^-{}_{aq} + HO_2^-{}_{aq}$	5.53×10^{-35} cm^6/s	Ref. [15][1]
$H_2O_{2aq} + H_2O_{aq} \rightarrow H_3O^+{}_{aq} + HO_2^-{}_{aq}$	1×10^{-21}	Ref. [15][1]
$H_3O^+{}_{aq} + HO_2^-{}_{aq} \rightarrow H_2O_{2aq} + H_2O_{aq}$	4.98×10^{-11}	Ref. [15][1]
$e(H_2O)_{aq} + O_2^-{}_{aq} \rightarrow OH^-{}_{aq} + HO_2^-{}_{aq}$	2.16×10^{-11}	[1]
$e(H_2O)_{aq} + O_3^-{}_{aq} \rightarrow OH^-{}_{aq} + OH^-{}_{aq} + O_{2aq}$	2.66×10^{-11}	[1]
$OH_{aq} + O_3^-{}_{aq} + H_2O_{aq} \rightarrow O_2^-{}_{aq} + O_2^-{}_{aq} + H_3O^+{}_{aq}$	3×10^{-34} cm^6/s	[1]
Reactive nitrogen species		
$HNO_{2aq} + H_2O_{aq} \rightarrow H_3O^+{}_{aq} + NO_2^-{}_{aq}$	3×10^{-20}	[1,3]
$HNO_{3aq} + H_2O_{aq} \rightarrow H_3O^+{}_{aq} + NO_3^-{}_{aq}$	3×10^{-18}	[1,3]
$H_3O^+{}_{aq} + NO_2^-{}_{aq} \rightarrow H_{aq} + NO_{2aq} + H_2O_{aq}$	6.81×10^{-10}	Based on pKa = 3.39[1]
$H_3O^+{}_{aq} + NO_3^-{}_{aq} \rightarrow HNO_{3aq} + H_2O_{aq}$	3.32×10^{-19}	Ref. [28][1]
$OH_{aq} + HNO_{3aq} \rightarrow NO_{3aq} + H_2O_{aq}$	2.17×10^{-13}	[1,4]
$H_{aq} + HNO_{2aq} \rightarrow NO_{aq} + H_2O_{aq}$	7.5×10^{-13}	[1,4]
$NO_3^-{}_{aq} + H_{aq} \rightarrow HNO_3^-{}_{aq}$	2.32×10^{-15}	[1]
$NO_3^-{}_{aq} + e(H_2O)_{aq} \rightarrow NO_3^{-2}{}_{aq} + H_2O_{aq}$	1.83×10^{-11}	[1]
$NO_3^{-2}{}_{aq} + H_3O^+{}_{aq} \rightarrow OH^-{}_{aq} + NO_{2aq} + H_2O_{aq}$	3.32×10^{-11}	[1]
$N_2O_{5aq} + H_2O_{aq} \rightarrow NO_{2aq} + NO_{3aq} + H_2O_{aq}$	1.46×10^{-19}	[2,4]
$ONOOH_{aq} + H_2O_{aq} \rightarrow H_3O^+{}_{aq} + ONOO^-{}_{aq}$	5×10^{-15}	[1,3]
$ONOO^-{}_{aq} + H_3O^+{}_{aq} \rightarrow H_2O_{aq} + ONOOH_{aq}$	1.75×10^{-6}	Based on pKa = 6.8[1]
$N_{aq} + H_2O_{aq} \rightarrow NH_{aq} + OH_{aq}$	6.93×10^{-39}	Based on T_{liquid} =

		300 K[2]
$H_{aq} + HNO_{aq} \rightarrow OH_{aq} + NH_{aq}$	2.18×10^{-22}	Based on T_{liquid} = 300 K[2,4]
$HNO_{4aq} + H_2O_{aq} \rightarrow NO_4^-{}_{aq} + H_3O^+{}_{aq}$	5×10^{-15}	[1,3]
$NO_4^-{}_{aq} + H_3O^+{}_{aq} \rightarrow HNO_{4aq} + H_2O_{aq}$	1.08×10^{-7}	Ref. [29][1]
$NO_4^-{}_{aq} \rightarrow NO_2^-{}_{aq} + O_{2aq}$	1.0 1/s	Ref. [29][1]
$HNO_{4aq} + HNO_{2aq} \rightarrow HNO_{3aq} + HNO_{3aq}$	1.99×10^{-20}	[1,4]
$HNO_{4aq} \rightarrow HNO_{2aq} + O_{2aq}$	7×10^{-4} 1/s	[1,4]
$HNO_{4aq} \rightarrow HO_{2aq} + NO_{2aq}$	4.6×10^{-3} 1/s	[1,4]
Carbon monoxide and carbon dioxide		
$CO_2(v)_{aq} + H_2O_{aq} \rightarrow CO_{2aq} + H_2O_{aq}$	5×10^{-15}	[1,3]
$CO(v)_{aq} + H_2O_{aq} \rightarrow CO_{aq} + H_2O_{aq}$	5×10^{-15}	[1,3]
$CO_{2aq} + H_{aq} \rightarrow CO_{aq} + OH_{aq}$	1.39×10^{-29}	Based on T_{liquid} = 300 K[2]
$CO_{2aq} + O_{aq} \rightarrow CO_{aq} + O_{2aq}$	1.21×10^{-49}	Based on T_{liquid} = 300 K[2]
$CO_{2aq} + H_2O_{aq} \rightarrow CO_{aq} + O_{aq} + H_2O_{aq}$	2.75×10^{-90}	Based on T_{liquid} = 300 K[2]
$O_2(^1\Delta)_{aq} + CO_{2aq} \rightarrow O_{2aq} + CO_{2aq}$	3×10^{-18}	[1]
$CO_2^+{}_{aq} + H_2O_{aq} \rightarrow H_2O^+{}_{aq} + CO_{2aq}$	5×10^{-15}	[1,3]
$CO_{aq} + H_2O_{aq} \rightarrow CO_{2aq} + H_{2aq}$	1.51×10^{-18}	Based on T_{liquid} = 300 K[2]
$OH_{aq} + CO_{aq} \rightarrow CO_{2aq} + H_{aq}$	1.24×10^{-13}	Based on T_{liquid} = 300 K[2]
$CO_{aq} + O_{2aq} \rightarrow CO_{2aq} + O_{aq}$	7.58×10^{-47}	Based on T_{liquid} = 300 K[2]
$CO_{aq} + HO_{2aq} \rightarrow OH_{aq} + CO_{2aq}$	1.48×10^{-27}	Based on T_{liquid} = 300 K[2]
$CO_{aq} + NO_{2aq} \rightarrow CO_{2aq} + NO_{aq}$	3.63×10^{-35}	Based on T_{liquid} =

		300 K[2]
$CO^+_{aq} + H_2O_{aq} \rightarrow H_2O^+_{aq} + CO_{aq}$	5×10^{-15}	[1,3]
Formate and sodium hydroxide		
$HCOOH_{aq} + OH_{aq} \rightarrow HCOO_{aq} + H_2O_{aq}$	2.16×10^{-13}	Ref. [27][1]
$HCOOH_{aq} + H_{aq} \rightarrow HCOO_{aq} + H_{2aq}$	1.01×10^{-13}	Ref. [27][1]
$HCOO^-_{aq} + OH_{aq} \rightarrow CO_2^-{}_{aq} + H_2O_{aq}$	5.31×10^{-12}	Ref. [27][1]
$HCOO^-_{aq} + H_{aq} \rightarrow CO_2^-{}_{aq} + H_{2aq}$	3.49×10^{-13}	Ref. [27][1]
$HCOO_{aq} + O_{2aq} \rightarrow CO_{2aq} + HO_{2aq}$	4.98×10^{-12}	Ref. [27][1]
$CO_2^-{}_{aq} + O_{2aq} \rightarrow CO_{2aq} + O_2^-{}_{aq}$	3.98×10^{-12}	Ref. [27][1]
$HCOOH_{aq} + H_2O_{aq} \rightarrow HCOO^-_{aq} + H_3O^+_{aq}$	1.66×10^{-20}	Ref. [15][1]
$HCOO^-_{aq} + H_3O^+_{aq} \rightarrow HCOOH_{aq} + H_2O_{aq}$	9.38×10^{-17}	Ref. [15][1]
$Na^+_{aq} + OH^-_{aq} \rightarrow NaOH_{aq}$	5×10^{-20}	[1,3]
$NaOH_{aq} + H_2O_{aq} \rightarrow Na^+_{aq} + OH^-_{aq} + H_2O_{aq}$	5×10^{-15}	[1,3]
Helium excited state solvation		
$M_{aq} + H_2O_{aq} + H_2O_{aq} \rightarrow He_{aq} + H_2O^+_{aq} + e(H_2O)_{aq}$ M = $He(2^1S)_{aq}$, $He(2^3S)_{aq}$, $He(2^3P)_{aq}$, $He(2^1P)_{aq}$, $He(3S)_{aq}$, $He(3P)_{aq}$	3.31×10^{-35} cm^6/s	[1,3]
$M_{aq} + H_2O_{aq} + H_2O_{aq} \rightarrow He_{aq} + H^+_{aq} + OH_{aq} + e(H_2O)_{aq}$ M = $He(2^1S)_{aq}$, $He(2^3S)_{aq}$, $He(2^3P)_{aq}$, $He(2^1P)_{aq}$, $He(3S)_{aq}$, $He(3P)_{aq}$	1.29×10^{-36} cm^6/s	[1,3]
$M_{aq} + H_2O_{aq} + H_2O_{aq} \rightarrow He_{aq} + H^+_{aq} + OH(A^2\Sigma)_{aq} + e(H_2O)_{aq}$ M = $He(2^1S)_{aq}$, $He(2^3S)_{aq}$, $He(2^3P)_{aq}$, $He(2^1P)_{aq}$, $He(3S)_{aq}$, $He(3P)_{aq}$	1.29×10^{-36} cm^6/s	[1,3]

$M_{aq} + H_2O_{aq} + H_2O_{aq} \rightarrow He_{aq} + H_{aq} + OH^+_{aq} + e(H_2O)_{aq}$ $M = He(2^1S)_{aq}, He(2^3S)_{aq}, He(2^3P)_{aq}, He(2^1P)_{aq}, He(3S)_{aq}, He(3P)_{aq}$	7.51×10^{-36} cm^6/s	[1,3]
$M_{aq} + H_2O_{aq} \rightarrow He_{aq} + H_{aq} + OH_{aq}$ $M = He(2^1S)_{aq}, He(2^3S)_{aq}, He(2^3P)_{aq}, He(2^1P)_{aq}, He(3S)_{aq}, He(3P)_{aq}$	1.25×10^{-12}	[1,3]
$He_2^*{}_{aq} + H_2O_{aq} + H_2O_{aq} \rightarrow H_2O^+_{aq} + He_{aq} + He_{aq} + e(H_2O)_{aq}$	1.98×10^{-34} cm^6/s	[1,3]
$He_2^*{}_{aq} + H_2O_{aq} + H_2O_{aq} \rightarrow H^+_{aq} + OH_{aq} + He_{aq} + He_{aq} + e(H_2O)_{aq}$	3.91×10^{-36} cm^6/s	[1,3]
$He_2^*{}_{aq} + H_2O_{aq} + H_2O_{aq} \rightarrow H^+_{aq} + OH(A^2\Sigma)_{aq} + He_{aq} + He_{aq} + e(H_2O)_{aq}$	3.91×10^{-36} cm^6/s	[1,3]
$He_2^*{}_{aq} + H_2O_{aq} + H_2O_{aq} \rightarrow H_{aq} + OH^+_{aq} + He_{aq} + He_{aq} + e(H_2O)_{aq}$	4.51×10^{-35} cm^6/s	[1,3]
$He_2^*{}_{aq} + H_2O_{aq} \rightarrow H_{aq} + OH_{aq} + He_{aq} + He_{aq}$	3×10^{-12}	[1,3]
$He^+_{aq} + H_2O_{aq} \rightarrow H_2O^+_{aq} + He_{aq}$	6.05×10^{-13}	[1,3]
$He^+_{aq} + H_2O_{aq} \rightarrow H_{aq} + OH^+_{aq} + He_{aq}$	2.86×10^{-12}	[1,3]
$He^+_{aq} + H_2O_{aq} \rightarrow H^+_{aq} + OH_{aq} + He_{aq}$	2.04×10^{-12}	[1,3]
$He^+_{aq} + H_2O_{aq} \rightarrow H^+_{aq} + OH(A^2\Sigma)_{aq} + He_{aq}$	5×10^{-15}	[1,3]
$He_2^+{}_{aq} + H_2O_{aq} \rightarrow He_{aq} + He_{aq} + H_2O^+_{aq}$	6.05×10^{-13}	[1,3]
$He_2^+{}_{aq} + H_2O_{aq} \rightarrow H_{aq} + OH^+_{aq} + He_{aq} + He_{aq}$	2.86×10^{-12}	[1,3]
$He_2^+{}_{aq} + H_2O_{aq} \rightarrow H^+_{aq} + OH_{aq} + He_{aq} + He_{aq}$	2.1×10^{-12}	[1,3]
$He_2^+{}_{aq} + H_2O_{aq} \rightarrow H_{2aq} + O^+_{aq} + He_{aq} + He_{aq}$	2.1×10^{-12}	[1,3]

$He_2^+{}_{aq} + H_2O_{aq} \rightarrow H_2^+{}_{aq} + O_{aq} + He_{aq} + He_{aq}$	2.1×10^{-12}	[1,3]
<u>Argon excited state solvation</u>		
$M_{aq} + H_2O_{aq} + H_2O_{aq} \rightarrow Ar_{aq} + H_2O^+{}_{aq} + e(H_2O)_{aq}$ $M = Ar(1s_1)_{aq}, Ar(1s_2)_{aq}, Ar(1s_3)_{aq}, Ar(1s_4)_{aq}$	3.31×10^{-33} cm^6/s	[1,3]
$M_{aq} + H_2O_{aq} + H_2O_{aq} \rightarrow Ar_{aq} + H^+{}_{aq} + OH_{aq} + e(H_2O)_{aq}$ $M = Ar(1s_1)_{aq}, Ar(1s_2)_{aq}, Ar(1s_3)_{aq}, Ar(1s_4)_{aq}$	1.29×10^{-34} cm^6/s	[1,3]
$M_{aq} + H_2O_{aq} + H_2O_{aq} \rightarrow Ar_{aq} + H^+{}_{aq} + OH(A^2\Sigma)_{aq} + e(H_2O)_{aq}$ $M = Ar(1s_1)_{aq}, Ar(1s_2)_{aq}, Ar(1s_3)_{aq}, Ar(1s_4)_{aq}$	1.29×10^{-34} cm^6/s	[1,3]
$M_{aq} + H_2O_{aq} + H_2O_{aq} \rightarrow Ar_{aq} + H_{aq} + OH^+{}_{aq} + e(H_2O)_{aq}$ $M = Ar(1s_1)_{aq}, Ar(1s_2)_{aq}, Ar(1s_3)_{aq}, Ar(1s_4)_{aq}$	7.51×10^{-34} cm^6/s	[1,3]
$M_{aq} + H_2O_{aq} \rightarrow Ar_{aq} + H_{aq} + OH_{aq}$ $M = Ar(1s_1)_{aq}, Ar(1s_2)_{aq}, Ar(1s_3)_{aq}, Ar(1s_4)_{aq}$	1.25×10^{-10}	[1,3]
$Ar_2^*{}_{aq} + H_2O_{aq} + H_2O_{aq} \rightarrow H_2O^+{}_{aq} + Ar_{aq} + Ar_{aq} + e(H_2O)_{aq}$	1.98×10^{-32} cm^6/s	[1,3]
$Ar_2^*{}_{aq} + H_2O_{aq} + H_2O_{aq} \rightarrow H^+{}_{aq} + OH_{aq} + Ar_{aq} + Ar_{aq} + e(H_2O)_{aq}$	3.91×10^{-34} cm^6/s	[1,3]
$Ar_2^*{}_{aq} + H_2O_{aq} + H_2O_{aq} \rightarrow H^+{}_{aq} + OH(A^2\Sigma)_{aq} + Ar_{aq} + Ar_{aq} + e(H_2O)_{aq}$	3.91×10^{-34} cm^6/s	[1,3]
$Ar_2^*{}_{aq} + H_2O_{aq} + H_2O_{aq} \rightarrow H^+{}_{aq} + OH^+{}_{aq} + Ar_{aq} + Ar_{aq} + e(H_2O)_{aq}$	4.51×10^{-33} cm^6/s	[1,3]

$Ar_2^*{}_{aq} + H_2O_{aq} \rightarrow H_{aq} + OH_{aq} + Ar_{aq} + Ar_{aq}$	3×10^{-10}	[1,3]
$Ar^+{}_{aq} + H_2O_{aq} \rightarrow H_2O^+{}_{aq} + Ar_{aq}$	6.05×10^{-11}	[1,3]
$Ar^+{}_{aq} + H_2O_{aq} \rightarrow H_{aq} + OH^+{}_{aq} + Ar_{aq}$	2.86×10^{-10}	[1,3]
$Ar^+{}_{aq} + H_2O_{aq} \rightarrow H^+{}_{aq} + OH_{aq} + Ar_{aq}$	2.04×10^{-10}	[1,3]
$Ar^+{}_{aq} + H_2O_{aq} \rightarrow H^+{}_{aq} + OH(A^2\Sigma)_{aq} + Ar_{aq}$	5×10^{-13}	[1,3]
$Ar_2^+{}_{aq} + H_2O_{aq} \rightarrow Ar_{aq} + Ar_{aq} + H_2O^+{}_{aq}$	6.05×10^{-11}	[1,3]
$Ar_2^+{}_{aq} + H_2O_{aq} \rightarrow H_{aq} + OH^+{}_{aq} + Ar_{aq} + Ar_{aq}$	2.86×10^{-10}	[1,3]
$Ar_2^+{}_{aq} + H_2O_{aq} \rightarrow H^+{}_{aq} + OH_{aq} + Ar_{aq} + Ar_{aq}$	2.1×10^{-10}	[1,3]
$Ar_2^+{}_{aq} + H_2O_{aq} \rightarrow H_2^+{}_{aq} + O_{aq} + Ar_{aq} + Ar_{aq}$	2.1×10^{-10}	[1,3]
$Ar_2^+{}_{aq} + H_2O_{aq} \rightarrow H_{2aq} + O^+{}_{aq} + Ar_{aq} + Ar_{aq}$	2.1×10^{-10}	[1,3]

[1]Added from to mechanism listed in Ref. [17].

[2]Rate coefficient changed from that in Ref. [17].

[3]Rate coefficient is estimated.

[4]From NIST Solution Kinetics Database. https://kinetics.nist.gov/solution/

Table 3. Henry's law constants [24].

Species	Dimensionless Henry's law constant	Note
Ar, Ar($1s_1$), Ar($1s_2$), Ar($1s_3$), Ar($1s_4$), Ar(4P), Ar(4D), Ar_2^*	3.47×10^{-2}	1,2
H, H^*	6.48×10^{-3}	1,2
H_2, H_2(r), H_2(v), H_2^*	1.80×10^{-2}	1
OH, OH($A^2\Sigma$)	6.20×10^{2}	1
HO_2	1.32×10^{5}	
H_2O_2	1.92×10^{6}	
H_2O(v)	1.00	2
O_2, O_2(v), O_2(r), $O_2(^1\Delta)$, $O_2(^1\Sigma)$	3.24×10^{-2}	1
O, O(^{1}D)	1.00	1
O_3, O_3^*	3.00×10^{-1}	1
N_2, N_2(r), N_2(v), $N_2(A^3\Sigma_u)$, $N_2(a'^1\Sigma)$, N, N(^{2}D)	1.60×10^{-2}	1,2
NO	4.40×10^{-2}	
NO_2	2.80×10^{-1}	
NO_3	4.15×10^{1}	
N_2O, N_2O(v)	5.99×10^{-1}	1
N_2O_3	6.00×10^{2}	
N_2O_4	3.69×10^{1}	
N_2O_5	4.85×10^{1}	
NH	1.47×10^{3}	3
HNO_2, HNO	1.15×10^{3}	1
HNO_3	4.80×10^{6}	
HNO_4	3.47×10^{6}	
CO, CO(v)	2.42×10^{-2}	1,2
CO_2, CO_2(v)	8.23×10^{-1}	1,2
He, He(2^3S), He(2^1S), He(2^3P), He(2^1P), He(3P), He(3S), He_2^*	9.42×10^{-3}	1,2

HCOOH, HCOO	1.25×10^5	[1]

[1] Value corresponds to the first species in the list, and other species listed were assumed to have the same Henry's law constant.

[2] Excited states rapidly quench to the ground state in reactions with water. As a result, the in-liquid density of the excited states is small, and there is rarely a limit to their transport into the liquid due to Henry's law consideration.

[3] Approximated by analogy to NH_3.

Table 4. Mole Fractions for Varying $HCOO^-_{aq}$ concentrations.

Species							
$HCOO^-_{aq}$ (mM)	0.5	1.0	2.0	3.5	5.0	7.5	10
OH^-_{aq} (10^{-9})	2.0	2.0	2.0	2.0	2.0	2.0	2.0
$H_3O^+_{aq}$ (10^{-9})	2.0	2.0	2.0	2.0	2.0	2.0	2.0
$HCOO^-_{aq}$ (10^{-5})	0.903	1.81	3.61	6.32	9.02	13.5	18.0
Na^+_{aq} (10^{-5})	0.903	1.81	3.61	6.32	9.02	13.5	18.0
$HCOOH_{aq}$ (10^{-10})	0.954	1.86	3.56	5.88	7.96	11.0	13.8
O_{2aq} (10^{-6})	4.98	4.98	4.98	4.98	4.98	4.98	4.98
N_{2aq} (10^{-6})	9.13	9.13	9.13	9.13	9.13	9.13	9.13

Table 5. Flow rates and corresponding residence times and reactive layer thicknesses.

Flow Rate (slm)	Residence Time (ms)	Reactive Layer Thickness (μm)	Note
0.75	13.5	7.0	Ref. [16]
1.0	10.0	6.0	Ref. [16]
1.25	9.2	5.8	[a]
1.5	8.3	5.5	Ref. [16]
1.75	7.4	5.2	[a]
2.0	6.4	4.8	Ref. [16]
2.5	5.7	4.5	[a]
3.0	4.9	4.2	Ref. [16]

[a] Residence time estimated by average.

Table 6. Powers for different gas mixtures.

Gas Mixture	Power (W)
He/H_2O = 99.8/0.2	14.3
He/O_2 = 99.8/0.2	14.2
$He/Ar/H_2O$ = 82.8/17.0/0.2	13.4
He	13.6
He/Ar = 83/17	5.3
He/H_2 = 99.8/0.2	13.6

Table 7. Comparison between experimental measurements and model results for the base case.

	Measurements [16]	Model Results
Electron density[1]	$(8.0 \pm 1.4) \times 10^{10}$ cm^{-3}	1.8×10^{11} cm^{-3}
Electron temperature[1]	3.8 ± 0.4 eV	2.6 eV
OH density[2]	3×10^{14} cm^{-3}	1.5×10^{14} cm^{-3}
$HCOO^-_{aq}$ concentration[3]	0.76 (± 0.15) mM	0.75 mM

[1]Value for model at 5 ms.

[2]Value for model at 10.1 ms (as the power begins to ramp down).

[3]Value for model at end of simulation.

Table 8. Comparison between experimental measurements and model results for different droplet diameters.

Droplet Diameter (μm)	Measured $HCOO^-_{aq}$ concentration (mM) [15,16]	Model $HCOO^-_{aq}$ concentration (mM)
36	0.77 (± 0.29)	0.64
41	0.76 (± 0.15)	0.75
56	1.61 (± 0.11)	1.02

Table 9. Comparison between experiments and model for different gas mixtures.

Gas Mixture	Measured OH density (cm^{-3}) [16]	Model OH density (cm^{-3})	Measured $HCOO^-_{aq}$ concentration (mM) [16]	Model $HCOO^-_{aq}$ concentration (mM)
He/H_2O = 99.8/0.2	3×10^{14}	1.5×10^{14}	0.76 (± 0.16)	0.75
He/O_2 = 99.8/0.2	--	2.4×10^{12}	0.80 (± 0.15)	0.71
$He/Ar/H_2O$ = 82.8/17.0/0.2	5×10^{14}	4.0×10^{14}	0.74 (± 0.10)	0.72

.

Figure Captions

1. a) Schematic of the experimental reactor. b) Schematic of the primary processes in the $HCOO^-_{aq}$ reaction mechanism.
2. $HCOO^-_{aq}$ concentration at the time of collecting the droplet for varying droplet reactive layer thicknesses at 1 slm flow rate. The concentration is averaged over the droplet.
3. Droplet and plasma properties for the base case. a) plasma properties, b) gas phase species densities, and c) liquid phase species densities in the reactive layer of the droplet.
4. OH, OH_{aq} and $HCOO^-_{aq}$ densities as a function of surface to volume ratio of the droplet. The densities of OH, OH_{aq} are when the power begins to ramp down (10.1 ms), corresponding to the droplet exiting the plasma. $HCOO^-_{aq}$ concentration is after an additional 10 ms, for flow to the collector. Aqueous quantities are averaged over the droplet.
5. Reactive species densities as a function of initial $HCOO^-_{aq}$ concentrations. OH and OH_{aq} densities are shown as the power begins to ramp down (10.1 ms) corresponding to the droplet leaving the plasma. $HCOO^-_{aq}$ concentration is shown after an additional 10 ms for flow to the collector. Aqueous quantities are averaged over the droplet.
6. Plasma properties as a function of gas flow rates. a) OH and OH_{aq} densities as the power begins to ramp down (droplet exciting the plasma) and b) $HCOO^-_{aq}$ concentration at the time of collection compared to experimental measurements from Nayak et al. [16]. Aqueous quantities are averaged over the droplet
7. OH, H_2O, and OH_{aq} densities as the power begins to ramp down (10.1 ms exiting the plasma channel) and $HCOO^-_{aq}$ concentration at the time of collection as a function of power. Aqueous quantities are averaged over the droplet
8. OH and OH_{aq} densities as the power begins to ramp down (10.1 ms, when the droplet exits the plasma) and $HCOO^-_{aq}$ concentration at the time of collection for different gas mixtures at 1 slm. Aqueous quantities are averaged over the droplet.
9. Droplet properties as a function of percentage of water in the inlet flow (He + X% H_2O). a) OH and OH_{aq} densities as the power begins to ramp down (8.4 ms, at exit of droplet from the plasma) at 1.5 slm compared to experimental measurements of OH from Oinuma et al. [15]. b) $HCOO^-_{aq}$ concentration at the time of collection compared to experimental measurements from Oinuma et al. [15]. Aqueous quantities are averaged over the droplet.